

# **Field-mediated Bioelectric Basis of Morphogenetic Prepatterning: a computational study**

**Authors:** Santosh Manicka<sup>1</sup> and Michael Levin<sup>1,\*</sup>

**Affiliations:**

<sup>1</sup> Allen Discovery Center at Tufts University, Medford, MA 02155, USA.

**\*Corresponding author:** [michael.levin@tufts.edu](mailto:michael.levin@tufts.edu)

**Running title:** Bioelectric Field Morphogenesis

**Keywords:** embryogenesis, morphogenesis, bioelectrics, field, pattern, complexity, information, dynamics, machine learning

## Abstract

Bioelectric communication among cells plays an important role in numerous morphogenetic processes. Computational modeling and experimental modulation of these processes have largely focused on a discrete, localized view of cells and intercellular networks determining spatio-temporal patterns of resting membrane potential ( $V_{\text{mem}}$ ) within tissues. Here we characterize novel contributions of the electrostatic force field, a continuous and pervasive entity existing within living tissues and modulating intercellular interactions. We consider a minimal but biologically-plausible non-neural bioelectric network model endowed with an electrostatic field where the  $V_{\text{mem}}$  of a cell is regulated by the average strength of the surrounding field via negative feedback. A detailed examination of this model revealed that the field systematically regulates key statistical and dynamical characteristics of spatiotemporal configurations of  $V_{\text{mem}}$  patterns such as complexity, dimensionality and causality by leveraging a mechanism akin to “synergetics” where it simultaneously forms a lower-dimensional projection of the pattern and enhances the causal strength and distance among its components. Moreover, the almost instantly-penetrating nature of the field endows the system with a unique amenability to self-organize complex positional information patterns following a transient stimulation of just the boundary of the tissue – an organizer-like property that suggests new avenues for modulation in biomedical contexts. We used automatic differentiation-based machine learning methods to optimize signals from a symmetry-breaking organizer region which would induce development of a vertebrate face prepattern. A detailed spatiotemporal dynamical analysis of a pair of such models with differing degrees of field-sensitivity revealed very different collective coordination strategies with which the model developed the pattern, namely, a ‘preformed’ mosaic mechanism and an ‘emergent’ stigmergic mechanism. The stigmergic pattern, in particular, recapitulated several key features of the developmental sequence of the bioelectric facial prepattern observed in frog embryos. These results highlight the promising potential of the electric field *per se* as a facilitator of collective patterning, providing a kind of master regulator interventional target for applications in regenerative medicine and bioengineering.

## Introduction

Biological control systems, such as the ones ensuring reliable, robust embryonic and regenerative morphogenesis [1-4], are an important and fascinating target of inquiry. Understanding these systems has direct relevance to the regenerative medicine of birth defects, injury, and cancer as well as to the fundamental dynamics of evolutionary developmental biology. One of their key features is the information flow that enables efficient control, especially via architectures in which coarse-grained “master regulator” variables serve as control knobs that facilitate highly coordinated, complex downstream effects. What kind of biophysical modality might underlie the integration and control of information across living tissue in space and time [5-9]?

Here we focus on the concept of “biological field”, originally formulated by pioneers such as Harold S. Burr, Alexander Gurwitsch, Henry Margenau and others during the early twentieth century as a response to Wilhelm Roux’s “mosaic theory of development” that was based on the philosophy of preformism [10-14]. Though the field concept has been adapted in several seemingly disparate forms, we apply its core idea, namely, an integrated, continuous, fluid, and invisible (to the naked eye) entity that regulates, and is regulated by, the relatively more segregated, discrete, rigid and palpable constituents of a biological system [1-5]. More commonly known as “morphogenetic field” in modern developmental biology, it expresses informational and regional relationships [15], the prototypical example of which is the morphogen gradient or the “French flag” model as is often referred to [16]. In his search for the core dynamics of substrate-invariant decision-making systems, Alan Turing proposed an early version of a *biochemical* basis of such a system, mimicking the self-organizing properties of embryos [9,17-23]. Here we develop an analogous *bioelectrical field* basis of patterning.

One important set of biological regulators concerns ionic signaling; all cells, not just neurons, communicate electrically *in vivo* [24,25]. Non-neural bioelectric signaling has now been implicated in embryogenesis, regeneration, and cancer suppression (reviewed in [26-28]). Bioelectric properties in tissue have been shown to underlie prepatterns regulating the formation of complex structures such as the vertebrate face [29,30], axial patterning of the anterior-posterior [31,32], dorso-ventral [33], and left-right [34,35] axes, the location and identity of specific organs such as the eye [36,37] and the egg-ovary system [38-42], patterning of epithelia such as skin and feathers [43], and size control [44-48].

Numerous gene expression [49] and epigenetic [50] targets lie downstream of changes in bioelectric state. Moreover, transduction machinery has been characterized for converting changes of cell resting potential into second messenger cascades that impact cell behavior such as migration, differentiation, and proliferation [51-53]. However, bioelectricity is fundamentally not a single-cell property; it has been argued [54,55] that its true import is because it reveals high-level, coarse-grained information structures that serve as master regulators for complex cascades of pattern formation. Indeed, modulation of resting potential via ion channel misexpression, pharmacological modulation of channels and pumps, and optogenetics has enabled triggering of whole organ formation [36], appendage regeneration [56], and tumor normalization [50,57]: spatio-temporal patterns of bioelectric

state across tissue trigger complex, organ-level downstream outcomes and all of the transcriptional changes that they require.

Thus, the bioelectric control system has been suggested as a promising therapeutic target for biomedicine [58-64], as well as an important component of the machinery of evolutionary changes in body structure and behavior [65-67]. Indeed, it is now becoming clear that modifying the bioelectric prepatterns observed in tissue, in accordance with the predictions of a computational model, can be modified to control downstream anatomy, such as repairing birth defects [68-70]. However, a fundamental capability gap is being able to induce desired bioelectric patterns. Because of the difficulty of establishing standing, long-term, spatially complex patterns of resting potential with electrodes, recent efforts have adopted a micromanagement strategy relying on computational models for picking electroceutical drugs (establishing patterns by turning channels on and off and relying on the downstream properties of the excitable medium of cells) [61,71,72]. Could including a field component in the models facilitate macroscale control of downstream bioelectric events via electrode methods, providing a new toolkit for regenerative medicine beyond the use of electrodes to target nerves [73,74]?

Although classic work in this field used the tools of applied and measured electric fields [75-82], more modern approaches have almost exclusively focused on the resting potential of individual cells [83-85] and the rules governing state transitions between neighbors and across tissue [86-93]. In effect, this agent-based, discrete approach mirrors a key conceptual workhorse in neuroscience – dynamics of neuronal networks and the patterns of information that propagate across these discrete networked nodes according to local interaction rules. It should be noted however, that a founding father of bioelectricity, Harold S. Burr, explicitly predicted that non-neural bioelectricity would not find its true depth of understanding and applications until its *field* aspect was incorporated, not just the particle aspect (the latter is how he referred to the discrete approach). Despite his warning in 1935 [94-98], very little work on incorporating actual electric fields into the quantitative modeling of endogenous developmental bioelectricity has been done. Likewise, the major approaches of targeting bioelectric controls for biomedical applications in morphogenesis have not exploited field concepts. However, the tide is shifting in neuroscience, with field aspects of neural function starting to take center stage as mediators of memory and long-range coherence [99-110]. Here, we explored the incorporation of true field aspects into bioelectric models of pattern generation.

What new features of morphogenetic control could a field contribute? We chose the electrostatic force field in the context of bioelectric cellular networks as a setting of a “continuous force field regulating and regulated by a discrete field of cells”, a picture that we believe not only captures the essence of the requirements of the concept of the field as described above but also potentially serves as a framework for the study of self-organization of coordinate system and positional information. We sought to characterize the role of the electrostatic force field in the patterning behavior of minimal bioelectric networks. For simplicity and tractability, we assumed that there is no intracellular or extracellular medium that could pose a hindrance to the transmission of the field via “charge screening” effects [111]. Furthermore, we have limited ourselves to relatively small cellular collectives and studied the general patterning behavior of two-dimensional lattice networks of a fixed 11x11

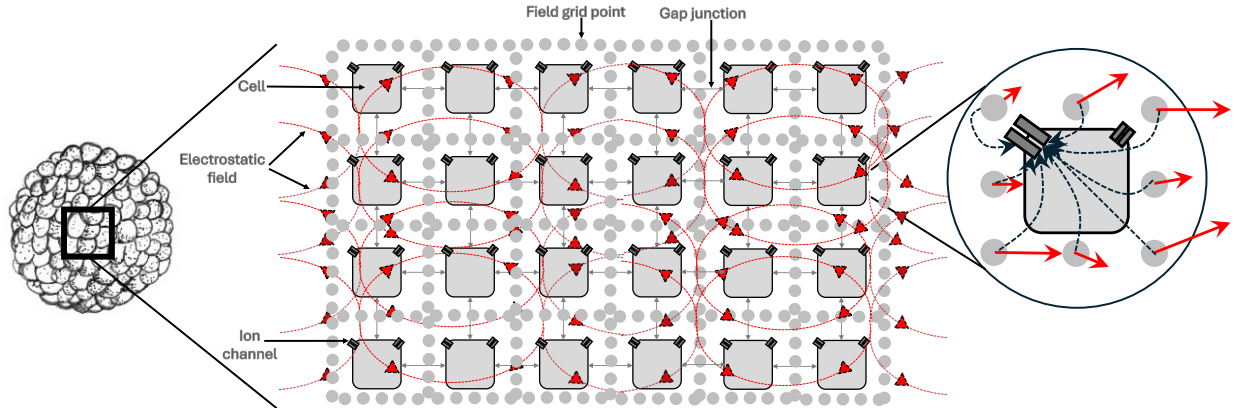
size under a variety of conditions representing the characteristics of the field. We then characterized examples of specific networks that generated complex patterns through self-organization primed by transient stimulation of a small part (boundary) of the tissue.

Figure 1 provides a schematic overview of the bioelectric field model of a 2-dimensional sheet of cells, such as the ectoderm that gives rise to the vertebrate face or brain. Each cell in the epithelium is equipped with a pair of generic voltage-gated ion channels (one that depolarizes the cell and the other that hyperpolarizes it). The cells are connected in style of a generic tissue lattice where neighboring cells are connected by voltage-gated gap junctions – electrical synapses known to play a critical role in shaping bioelectric signaling [112-114] as well as the movement of other physiological small molecules. This core model, that has been adopted in several studies before [87,92,93,115-121], is further endowed with an electrostatic field induced by the collective of the net charges or the membrane potentials ( $V_{\text{mem}}$ ) of the cells. Motivated by several “electroreception” mechanisms (the phenomenon by which an organism perceives electric fields through special “electroreceptors”) observed in nature, ranging from atoms to entire ecosystems [122], and specific electric field transduction mechanisms employed by cells [123-126], we equipped our model with a transduction mechanism where the average magnitude of the electrostatic forces that a cell perceives modulates its ion channel opening. Specifically, if the net force exceeds a certain transduction threshold, then the polarizing channel begins to gradually constrict causing the cell to depolarize more (details in Methods). Furthermore, the extent of the spatial reach of the electrostatic field radiated by a cell is controlled by the parameter called ‘action range’ (see red boxes in top row of Figure 2). The corresponding ‘perception range’ of a cell (blue boxes in top row of Figure 2), defined as the region around it within which the cell can measure the field, is fixed to the size of the cell itself. That is, a cell can only perceive the field impinging on its surface. In summary, the model is defined by four parameters: gap junction strength (G), field transduction weight (W), field transduction threshold (B) and field action range (R).

The electrostatic force fields follow Coulomb’s laws and conventions: the magnitude of the force due to the field emitted by a cell shrinks in proportion to the inverse square of the distance from the cell, and the force vectors are pointed to the cell if it is negatively charged (top row of Figure 2). When multiple cells emit fields the net force at each point in the tissue is obtained by vector addition of the contributions of forces from all cells (bottom row of Figure 2). The static snapshot of the force field profile of the tissue is determined only by the spatial distribution of  $V_{\text{mem}}$  and R. The parameters R, W and B, play a role in the dynamical behavior of patterning. Models with a high W and low B have strong field sensitivity and those with a low W and high B possess weak field sensitivity. The combination of field sensitivity strength and R result in different types of patterns with varying degrees and spatial configuration of contrast, examples of which are shown in Figure 3.

We used this model to ask several specific questions about the ways in which true field dynamics might impact the contribution of bioelectrical mechanisms to morphogenesis, and in the interactions between the roles of the field and the “particle” ( $V_{\text{mem}}$ ) components. We find that the presence of the field in an otherwise conventional bioelectric system indeed enhances its patterning capabilities, an effect that was quantified in terms of pattern complexity, dimensionality and causal catalysis. This effect was achieved in the system via

the emergence of the field as an effective control parameter that catalyzes causal interactions among the cells thereby driving tissue patterning. Lastly, we exploited this mechanistic understanding of the bioelectric field system to prime it to develop a specific target pattern – the vertebrate face. We achieved this simply by stimulating the field around boundary of the tissue using an oscillatory paradigm, the sequence of which was optimized using machine learning.



*Figure 1.* Illustration of the model. The target of the model is a portion of an early stage embryo such as the blastula (left), modeled as a simple 2D lattice network of bioelectric cells equipped with an electrostatic field that is collectively induced by the  $V_{mem}$  of the cells (center) that in turn interacts with the  $V_{mem}$  of individual cells (right). Grey squares represent cells, with the black marks at the top corners of each cell representing the two ion channels. The thin double headed grey arrow marks connecting neighboring cells represent gap junctions. The small grey circles represent the field grid points, and the red arrows passing through them and the cells represent the electrostatic field lines. The zoomed in view of a cell on the right more clearly shows the force vectors on each field grid point (red arrows) and their modulatory effect on the ion channel (black dashed arrows).

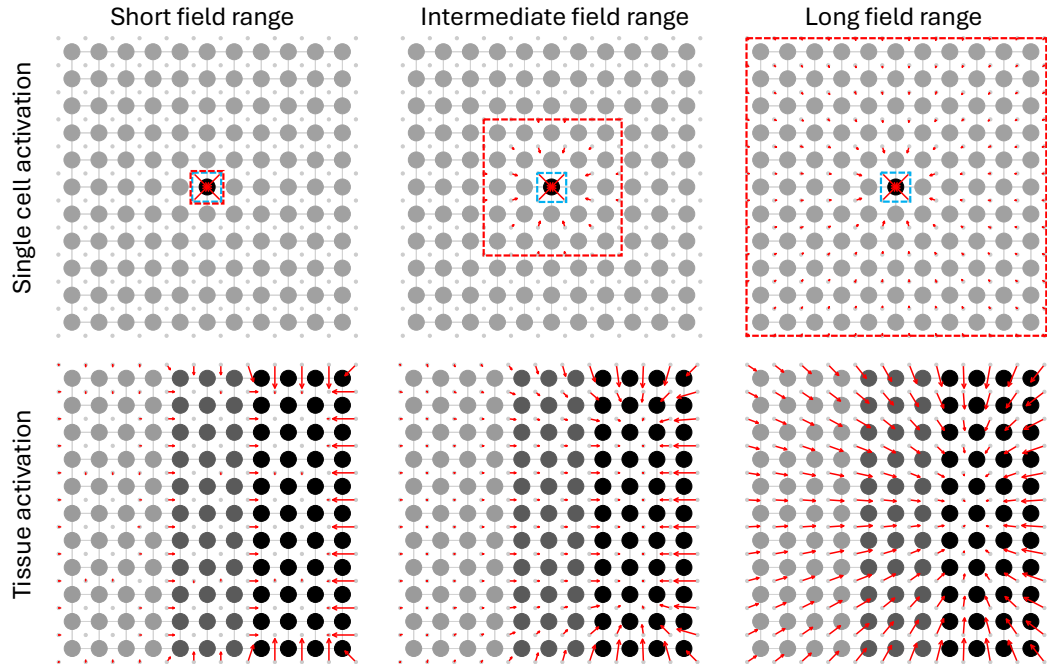


*Figure 2.* Static snapshots of the electrostatic force field profiles of the model when a single cell is active (top row) and when the entire tissue is voltage-patterned (bottom row) under differing extents of the field action range (columns). In the

top panels, the blue dashed squares represent the field perception range and the red dashed squares represent the field action range. The red arrows in all panels represent the force vectors at the field grid points. The shades of the cells represent the voltage states, with darker shades representing more hyperpolarized potentials.

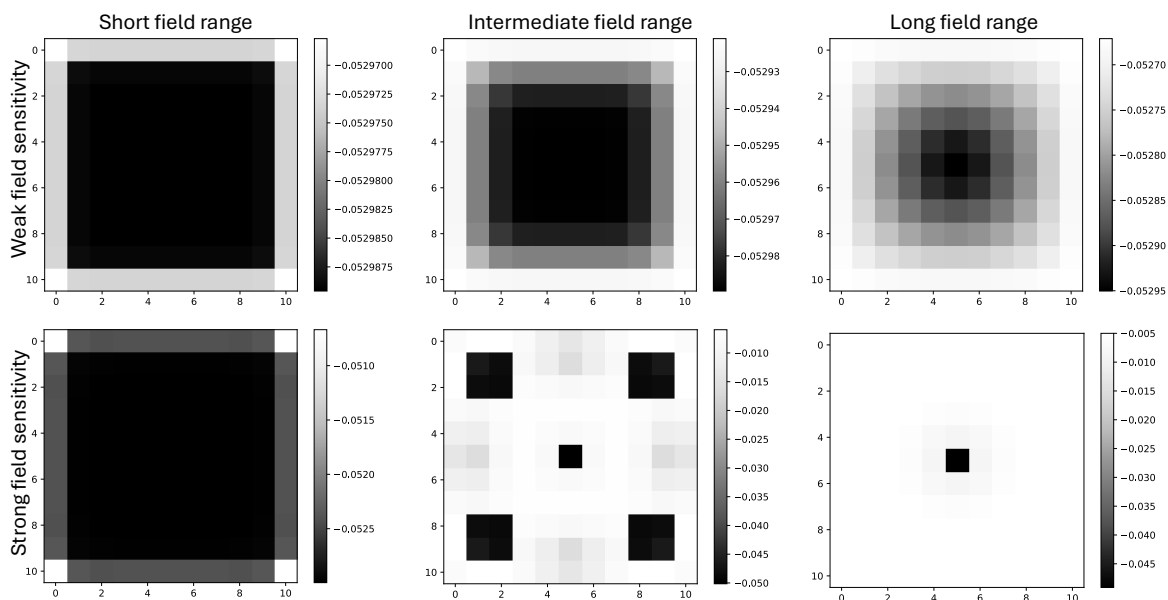


**Figure 3.** Patterns generated by the 11x11 model under various field transduction conditions. Top row panels show models with weak field sensitivity (low W and high B), and the bottom row panels represent strong field sensitivity (high W and low B). Columns represent models with different field action ranges, namely, short, intermediate and long ranges. Patterns displayed are obtained after 1000 steps of simulation each starting from homogenous initial conditions (details in Methods). Shades represent voltage states with darker shades representing more hyperpolarized potentials.

## Results

### Bioelectric field enhances the complexity of voltage patterns in the tissue

Embryos employ a variety of biomolecular mechanisms, such as diffusion, reaction-diffusion and vector transport, as well as bioelectric pre-patterning mechanisms to self-organize develop positional information patterns during the course of development [15,16,92,127-129]. Here we ask: could the electrostatic field endow the bioelectric machinery with an enhanced capacity to pattern?

To determine this, we considered the Tononi-Edelman-Sporns complexity measure (TSE) of the  $V_{\text{mem}}$  patterns [130]. TSE is an information-theoretic quantity that quantifies the tradeoff between integration and segregation of the  $V_{\text{mem}}$  patterns at multiple spatial scales. It is defined as the total sum of mutual information between bipartitions of the system covering all partition sizes (details in Methods). When the tissue is fully integrated the cells tend to behave synchronously as a single whole, and when it is fully segregated the cells tend to behave independently – TSE is zero in both cases. Complexity is maximized when the balance between the opposing forces of integration and segregation is maximized, which is precisely what a good patterning mechanism must possess since a pattern, by definition, requires a mixture of correlated and uncorrelated regions.

We simulated an ensemble of models by sweeping its parameter space consisting of G, W, B and R, representing the gap junction strength, field transduction weight and threshold

and field action range respectively (details in Methods). For each parameter combination, we computed the TSE of the corresponding model as the average over a set of 100  $V_{\text{mem}}$  timeseries each obtained from a randomly chosen initial  $V_{\text{mem}}$  configuration and run for 5000 steps. Since TSE is typically over binary probability distributions (as inferred from timeseries data) and given that the cells of our model are bistable, we computed the TSE over the binarized  $V_{\text{mem}}$  timeseries (details in Methods).

The results (Figure 4) revealed that models with stronger field sensitivities display higher values of TSE ( $80 \pm 20$  bits) whereas models with weaker field sensitivities display relatively lower TSE values varying in the range 0-30 bits. For comparison, the expected TSE of a randomly generated pattern timeseries is 0 bits (no correlations between partitions on average) and a model without a field would behave like models with zero field sensitivity, possessing TSE values close to 0 bits. Furthermore, scenarios with stronger field sensitivities (top right region of Figure 4) possess an optimal FR where TSE maximizes, the value of which depends on the corresponding parameter combination. For example, the optimal FR for models with  $W=1000$  and  $B=0.0005$  ranges between short and intermediate ranges (1 to 4) that then expands to a range of 15 to 21 as the transduction threshold rises. These observations make sense since a higher threshold means that a cell needs to be responsive to a larger section of the tissue in order to assimilate their activities in its contribution to the complexity of the whole. Models with weaker field sensitivities (bottom left region of Figure 4) tend to behave in a linear fashion since the cells respond less to changes in the activities of neighboring cells due to the dampened field-mediated communication, as a result of which the complexity of the patterning is reduced regardless of the field range.

Our results constrain the threshold electrostatic force required for complex patterning to an approximate range of 0.0005 mV/mm to 0.005 mV/mm (estimated by the multiplying  $W$  with  $B$  and dividing by 1000 to convert length units from meter to millimeter) which is about 100 times smaller than the theoretically expected and empirically observed value of about 0.1 mV/mm [131,132]. However, the corresponding magnitudes of the electrostatic potential observed in our model is about 1% of the magnitudes of the corresponding  $V_{\text{mem}}$  (which ranges between -5 to -55 mV), matching empirical observations. Both of these ratios can be easily manipulated in our model by adjusting the relative permittivity of the cell (see model definition in Methods) without changing the qualitative landscape of the results plotted in Figure 4, but matching one metric would occur at the cost of the other. The other interesting correspondence with biology is that the optimal field range is quite small for the strongly sensitive models, matching biological observations that the reach of the field is limited to small regions around the cells due to ‘field screening’ effects [111].

In summary, these observations show that endowing a conventional bioelectric system with an electrostatic field enhances its patterning capacity, as evidenced by an increase in the complexity of the  $V_{\text{mem}}$  patterns with an increase in the ability of the cells to sense changes in the field surrounding them.



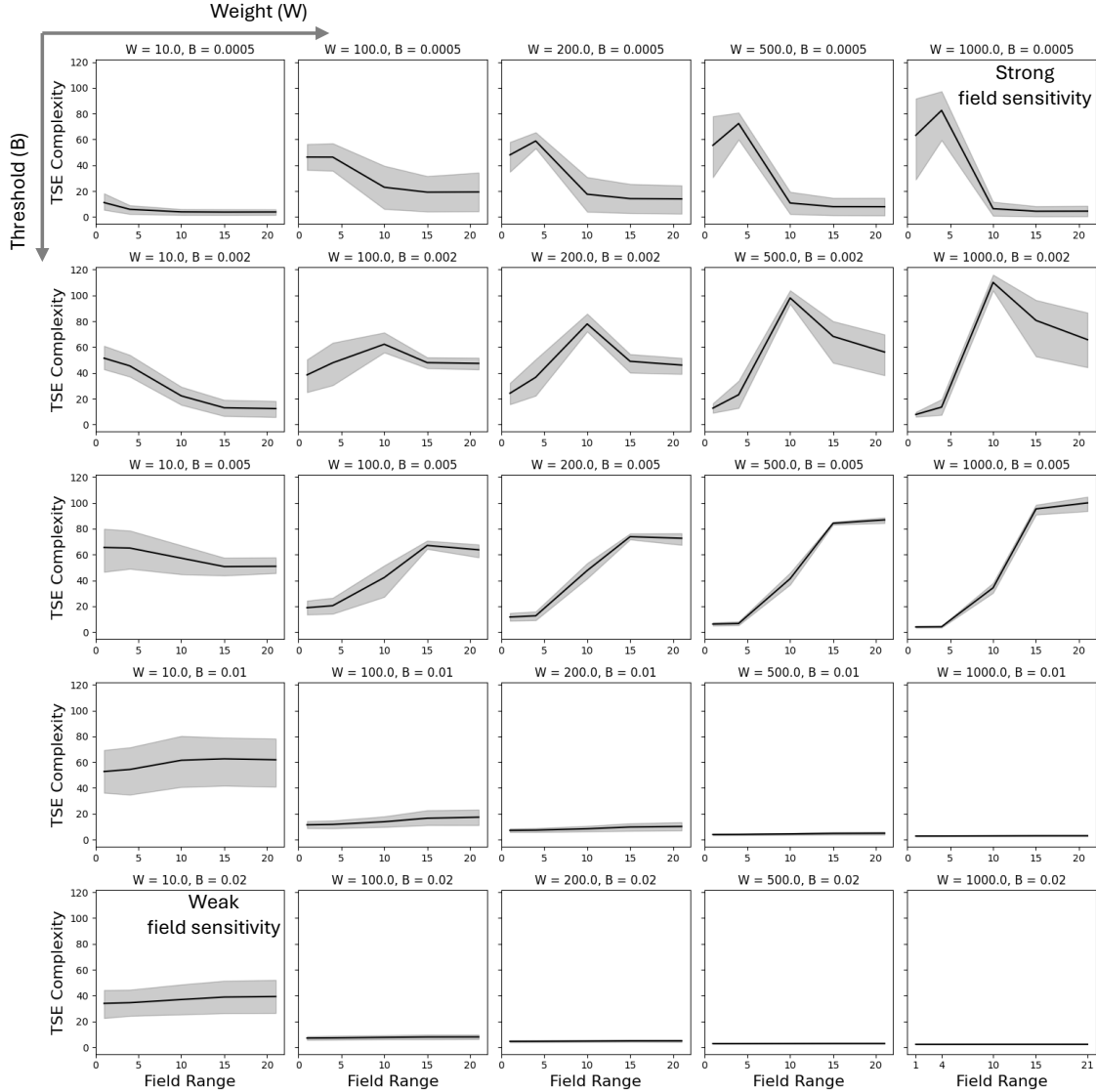


Figure 4. TSE complexity of  $V_{mem}$  patterns as a function of  $R$ ,  $W$  and  $B$ . Values were calculated for each parameter combination ( $G$ ,  $R$ ,  $W$  and  $B$ ) as the mean taken over 100 model instances consisting of hundred randomized initial conditions simulated for 5000 steps. Error bands represent the 95% confidence interval around the mean estimated using nonparametric bootstrapping. Variations are due to differences in  $G$  that was averaged over.

### Bioelectric field controls $V_{mem}$ activity using a mechanism akin to synergetics

Electric fields play a critical role in shaping cognition and memory in the brain, as evidenced by recent research showing that the simian brain uses electric fields to stabilize memory formation and recall [99]. The brain does so by leveraging the slower timescale, lower dimensionality and higher stability of the electric field to effectively purpose it as a controller of neural activity despite their recurrent relationship [99-101]. This is akin to a principle described by Hermann Haken in his theory of “synergetics” stating that the dynamics of fast modes is determined (“enslaved”) by the slow modes [133]. Could viewing morphogenesis through the lens of cognition [134] reveal similar underlying principles of

morphogenetic patterning, an idea that was also speculated elsewhere [133]? In the specific context of our model of *non-neural* tissue, could the electric field perform an analogous role of controlling  $V_{\text{mem}}$  activity by acting as its “guardrail” [99]?

To answer it, we considered the following measures (details in Methods): 1) “relative field compression” (RFC), defined as the difference between the total variance explained by the first three “principal component axis” (PCA) dimensions of the field and the  $V_{\text{mem}}$  timeseries and expressed in the dimensionless units of percentage; and 2) “field influence” (FI), defined as the rate of change of  $V_{\text{mem}}(v)$  with respect to small changes in the electrostatic force (V/m) between arbitrary cells and field grid points, expressed in units of distance (m) representing the displacement of the cell if the change in its electric potential energy were to be converted into kinetic energy. The first measure expresses the extent to which the field is more or less compressed and thus its temporal variability compared to the  $V_{\text{mem}}$  pattern, while the second measure expresses the degree of control the field exerts over the  $V_{\text{mem}}$  pattern (equivalently, the amount of energy it injects into it). Together, these measures quantify the extent to which the system displays synergetic effects, where the field acts as a slower timescale control ‘parameter’ and  $V_{\text{mem}}$  acts as a faster enslaved ‘parameter’ (analogous to neural activity as described above).

As before, we constructed an ensemble of models by sweeping its parameter space consisting of G, W, B and R (details in Methods) and for each parameter combination we computed RFC and FI of the corresponding model as the average over a set of 100 timeseries each obtained from a randomly chosen initial  $V_{\text{mem}}$  configuration and run for 5000 steps (details in Methods).

We found that RFC peaked at about  $35\% \pm 5\%$  for models with stronger field sensitivity and dropped to a range of -5% to 5% for models with weaker field sensitivity (Figure 5). It moreover, stayed positive for the stronger models but sometimes became negative for the weaker models. In other words, the field not only generally tends to be more compressed than  $V_{\text{mem}}$  for the strongly sensitive models but also their difference tends to be higher compared to the weakly sensitive models. Besides, the optimal field range where RFC maximizes follows the same trend as what was observed for TSE above, in that among the strongly sensitive models a lower transduction threshold meant a shorter optimal field range, whereas a higher threshold meant a longer optimal field range. A higher compression of the field is manifest in its slower variation (see Supplementary Material Figures S1-S3), meaning that strongly sensitive models display slower variations in the field. The reason for this is that small changes in the field trigger large changes in the  $V_{\text{mem}}$  activity but by the time the field catches up it steps past the threshold and the  $V_{\text{mem}}$  starts swinging in the other direction (due to negative feedback and bistability).

The qualitative trend in the behavior of FI was found to be similar to RFC across the parameter space, achieving a peak of about  $3.5 \text{ mm} \pm 0.5 \text{ mm}$  in the strongly sensitive models and dropping to 0 mm for in the weakly sensitive ones and displaying shorter optimal field ranges for the stronger models and longer ranges for the weaker models. The only exception occurred at the parameter combination of (W=1000, B=0.002) where the optimal field range narrowly peaked at a value of 10 with respect to FI, whereas almost all field ranges beyond 10 were equally optimal with respect to RFC. Notwithstanding that exception, we

can safely conclude that RFC and FI behave similarly in response to changes in model parameters.

These results suggest that models with stronger field sensitivity indeed display effects akin to synergetics, in that the field effectively acts as a causal control parameter of  $V_{\text{mem}}$  activity due to its relatively slower timescale, less variability and higher stability.

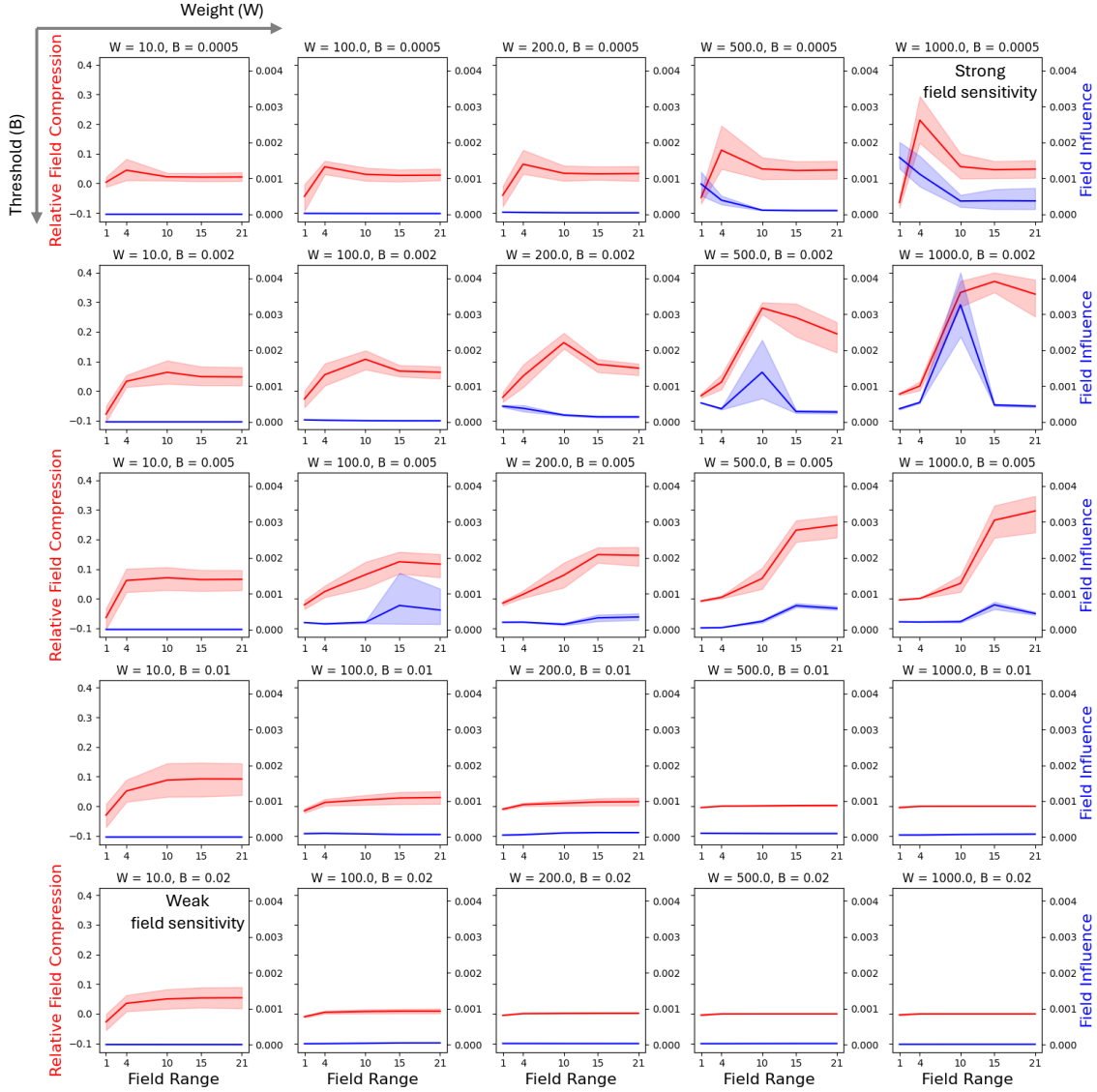


Figure 5. Relative field compression and field influence as a function of R, W and B. Red lines indicate RFC values and are plotted against the left y-axis and blue is FI plotted against the right y-axis. Values were calculated for each parameter combination (G, R, W and B) as the mean taken over 100 model instances consisting of hundred randomized initial conditions simulated for 5000 steps. Error bands represent the 95% confidence interval around the mean estimated using nonparametric bootstrapping. Variations are due to differences in G that was averaged over.

## Bioelectric field catalyzes non-local causal interactions among the cells constituting the $V_{\text{mem}}$ pattern

Long-distance signaling plays a crucial role in morphogenesis, facilitating spatiotemporal coordination among the parts of the developing system [135]. Some of the major sources of long-distance communication that have been so far identified include diffusing morphogens, cellular protrusions, tunneling nanotubes, macrophage networks as well as bioelectric signaling [136-138]. Electric fields are also known to play a role during development in the form of cell migration (galvanotaxis), proliferation and modulation of ion channels [123,135,139]. Could the electric field also facilitate direct cell-to-cell communication especially at long distances even if it is weak? In the context of our model, could the field catalyze the interactions among the components of the  $V_{\text{mem}}$  pattern despite being orders of magnitude smaller (about 1%) than  $V_{\text{mem}}$ ?

To answer this question, we considered measures that express the degree and length of causal interactions between the cells facilitated by the field across space and time. Accordingly, we defined causal strength (CS) and causal distance (CD) respectively as (details in Methods): 1) the absolute value of the derivative of the  $V_{\text{mem}}$  of three representative target cells of the tissue at representative time points  $t > 0$  of the simulation with respect to the  $V_{\text{mem}}$  of every cell at  $t = 0$ , averaged over target cells and time and expressed in dimensionless units; and 2) the distance corresponding to the highest causal strength, averaged over target cells and time and expressed in units of distance (m). Causal strength quantifies the sensitivity of the  $V_{\text{mem}}$  of a cell to small changes in the  $V_{\text{mem}}$  of another cell separated in space and time, and causal distance indicates the distance at which it occurs.

As before, we constructed an ensemble of models by sweeping its parameter space consisting of  $G$ ,  $W$ ,  $B$  and  $R$  (details in Methods) and for each parameter combination we computed CS and CD of the corresponding model over a single simulation trajectory initiated with homogenous conditions and run for 500 steps (details in Methods).

The results (Figure 6) revealed that CS maximized to about  $0.002 \pm 0.0005$  for models with relatively stronger field sensitivity, dropping to zero for models with weaker field sensitivity. As with TSE, RFC and FI above, CS also maximized at shorter field ranges for strongly sensitive models with a lower transduction threshold and at longer ranges for similar models but with higher thresholds – likely due to the same reasons as before. Likewise, CD maximized at about  $30 \mu\text{m}$  (about 3 cells wide) for models with relatively stronger field sensitivity, sometimes rising to  $90 \mu\text{m}$  (about 9 cells wide), and dropping to zero for models with weaker field sensitivity.

The above results indicate that small changes at the beginning of the simulation in the  $V_{\text{mem}}$  of a cell could cause changes up to 2 mV in another cell about 9 cells away from the source after 500 steps in models with strong field sensitivity. An important implication of the above results is that causal strength does not necessarily decrease monotonically with causal distance. That is, the strongest causal influence does not necessarily stem from the closest cells but from cells further away. Taken together, our results show that the electric field indeed has the potential to catalyze non-local causal interactions among cells, in a way that is not a simple linear function of distance – a phenomenon that is crucial for morphogenetic patterning and its control.

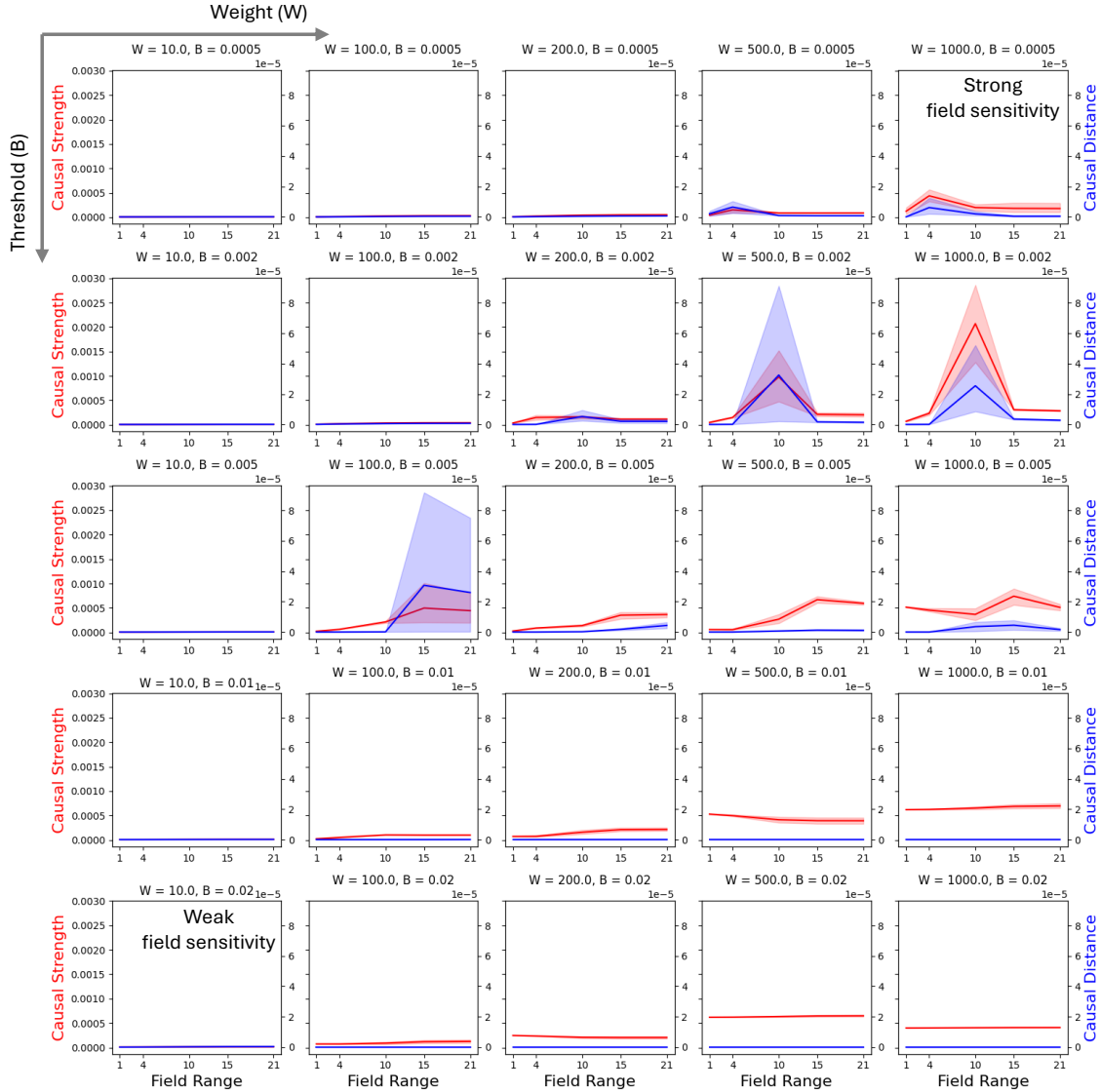


Figure 6. Causal strength and causal distance as a function of field range. Red lines indicate CS values and are plotted against the left y-axis and blue is CD plotted against the right y-axis. Values were calculated for each parameter combination (G, R, W and B) as the mean taken over 100 model instances consisting of hundred randomized initial conditions simulated for 5000 steps. Error bands represent the 95% confidence interval around the mean estimated using nonparametric bootstrapping. Variations are due to differences in G that was averaged over.

### Bioelectric field facilitates the development of a vertebrate face $V_{mem}$ pattern in the bulk of the tissue following transient stimulation of just its boundary by employing mosaic and stigmergy-based strategies

Several morphogenetic processes observed in embryos are initiated by a so-called “organizer” – a region that supplies positional information to distant cells [140-142]. Could the electric field facilitate such patterning through transient stimulation of a small part of the tissue? Moreover, several known morphogenetic patterning processes in embryos adopt a linear and direct decoding strategy where most of the information about the pattern is supplied by the morphogens or are deduced using relatively simple interpretation processes

such as the French flag and the clock-and-wavefront mechanisms [143]. Could there be more nonlinear and complex strategies where the initial information supplied by an organizer-like entity is coded and the system actively decodes it to generate the full pattern? Motivated by these questions, we asked: could we prime our model to bootstrap a full vertebral face pattern in the bulk of the tissue by stimulating only its boundary?

To study this, we designed a procedure to learn the appropriate stimulation values required for generating a face-like  $V_{mem}$  pattern following a transient stimulation of only the field grid points located around the boundary of the tissue. For this purpose, we chose a pair of field transduction parameter sets corresponding to the strongly sensitive and weakly sensitive categories for this purpose with the goal of sampling the extremes of a potential range of patterning strategies that the system might employ. Specifically, we chose the parameter combinations ( $W=1000$ ,  $B=0.0005$ ) and ( $W=10$ ,  $B=0.02$ ) with the field range set to 4 and the gap junction strength set to 0.05. We set  $R$  to 4 since that's one of the most optimal parameters of the model, as can be seen in the results above.

We adopted an oscillatory paradigm to stimulate the boundary due to its potential ability to facilitate complex patterning via wave superpositions in the bulk – an approach inspired by phenomena such as cymatics [144] and bulk-boundary correspondence of the holographic principle [145]. However, in order to emulate embryogenic patterning, the stimulations were designed to be transient and last for only an initial fraction (10%) of the simulation time (1000 steps). We used a machine learning algorithm called gradient descent [146] to learn the optimal values of the oscillatory inputs, namely, the amplitudes and frequencies of the inputs meant to be applied on each of the field grid point situated around the boundary of the tissue (details in Methods). A demonstration of the steps involved in the patterning is shown in Figures 7 and 8 corresponding respectively to the weakly sensitive and strongly sensitive models.

Figure 7 reveals that following the brief stimulation period ( $t=100$ ) the weakly sensitive tissue is left in what could be conceived as a pre-pattern consisting of a vague outline of a smiley that then sharpens into the full smiley pattern at  $t=1000$ . The corresponding force field profiles suggest a linear decoding strategy where each region of the pattern, namely the skin, eyes, nose and mouth simply increasingly hyperpolarize without involving any intricate mechanism of coordination. This is evident upon visual inspection when at  $t=100$  the field vectors point weakly to the features of the pattern, then at  $t=800$  they all point to the boundary since the cells there are the first ones to hyperpolarize, and finally at  $t=1000$  when all the features respectively hyperpolarize the field vectors immediately surrounding them point towards them.

Figure 8 shows that the strongly sensitive model follows a very different strategy compared to the weakly sensitive model above. The first difference can be observed in the pattern left in the tissue at the end of stimulation ( $t=100$ ) that bears no resemblance to the smiley; in fact, the pattern in the bulk is just a monotonic pattern that increasingly hyperpolarizes towards the center of the tissue. The more important difference is that the rest of the simulation involves a stigmergic communication between the parts of the bulk and the boundary that literally sculpts the features of the smiley through a sequence of what we call “field bifurcation” steps. For instance, at  $t=700$ , as the cells at the center hyperpolarized, the boundary cells directly to their left and right also hyperpolarized even

though the cells the top side of the boundary were more bound to hyperpolarize at  $t=100$  (should they have followed a linear strategy they would have hyperpolarized first at  $t=700$ ). Notice that the cells in between them don't hyperpolarize, resulting in a local bifurcation of the field. The newly hyperpolarized cells further trigger cells in the top portion of the bulk to hyperpolarize that then trigger other boundary cells and so on until the smiley is almost complete at  $t=1000$ . For these reasons, we will henceforth refer to the weakly sensitive patterning model as the 'mosaic' model and the strongly sensitive model as the 'stigmergic' model.

To test the hypothesis that bulk-boundary communication drives the patterning in the stigmergic model but not in the mosaic model, we measured the following: 1) normalized mutual information between the bulk and the boundary ( $\widehat{MI}$ ); 2) causal strength of interactions flowing from the boundary to the bulk ( $\widehat{CS}$ ); and 3) degree of deformity in the pattern caused due to permutation of the boundary states ( $\Delta D$ ) in both models (details in Methods). We found that both  $\widehat{MI}$  and  $\widehat{CS}$  were indeed stronger in the stigmergic model, with  $\widehat{MI}$  about 3.5 times stronger and  $\widehat{CS}$  twice as strong, and whereas  $\Delta D$  was on average about 44.5% for the stigmergic model but 0% for the mosaic model, meaning that perturbing the boundary states resulting in significant developmental deformities in the former but not in the latter (Table 1). We also measured RFC that was about thrice as strong in the stigmergic model as in the mosaic model, suggesting that the bulk-boundary interaction is not only higher but also more synergetic in the former.

It should be noted that the mosaic model required orders of magnitude stronger input voltages (see Supplementary Material Figure S4). These conditions make sense because a weakly sensitive model requires stronger external inputs to supply almost all of the information about the target pattern (in the form of a pre-pattern), as it cannot leverage the field strongly enough to complete the pattern. A higher field-sensitivity of a strongly sensitive model, on the other hand, allows it to rely on only weak external inputs to bootstrap complex patterns by utilizing the field as a scaffold. This facilitates the model to employ mechanisms such as stigmergy that require minimal information to be supplied initially that may be sufficient to prime the nonlinearity of the system to take over and guide it in the direction of the desired outcome.

These results demonstrate that the bioelectric field can indeed allow the model to be dynamically molded into complex patterns by priming its self-organization through transient stimulation of only the boundary of the tissue, thus circumventing the need for micromanagement that several contemporary interventional patterning methodologies entail (e.g., ion channel modulation [70]).

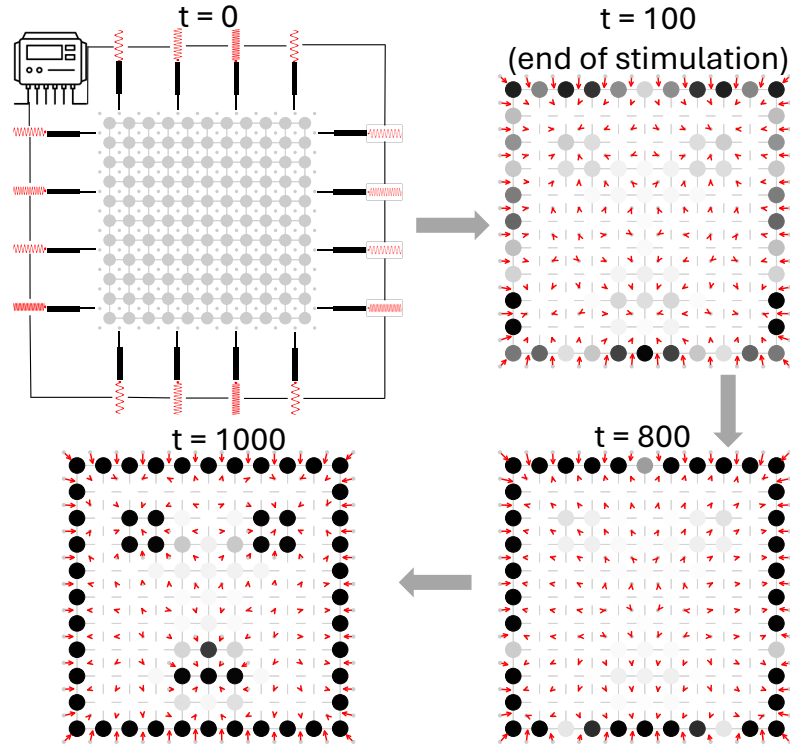


Figure 7. Development of the face pattern in the mosaic model shown as a sequence of snap shots of the combined  $V_{mem}$  and force field profile. This model has the following fixed set of parameter values:  $R = 4$ ,  $G = 0.05$ ,  $W = 10$  and  $B = 0.0283$ . The only values that were optimized using machine learning were the amplitudes and frequencies of the initial transient stimulation. At  $t=0$ , the oscillatory stimulation is applied and continued until  $t=100$ . The full pattern is formed at  $t=1000$ . The profile at an intermediate timepoint of  $t=800$  is also shown. Lighter shades of the cells represent cells depolarized potentials of about -5 mV and darker shades correspond to hyperpolarized potentials of about -55 mV. Red arrows indicate force field vectors at the field grid points.



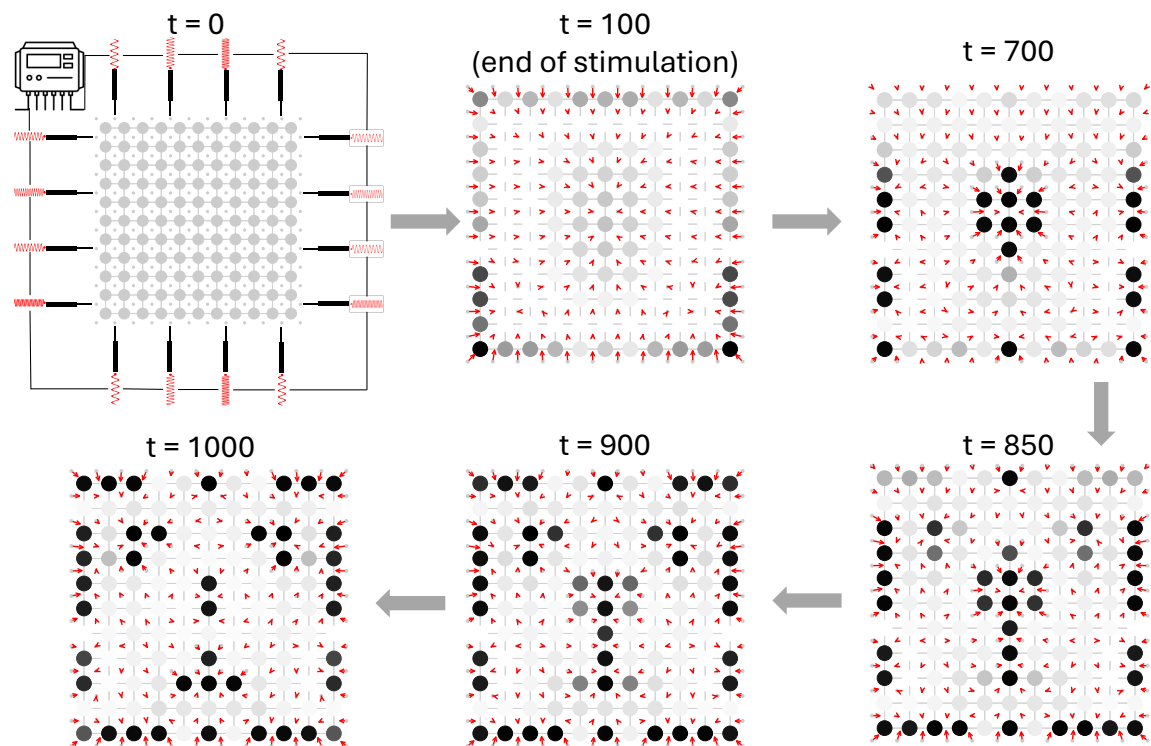


Figure 8. Development of the face pattern in the stigmergic model shown as a sequence of snap shots of the combined  $V_{mem}$  and force field profile. This model has the following fixed set of parameter values:  $R = 4$ ,  $G = 0.05$ ,  $W = 1000$  and  $B = 0.0005$ . The only values that were optimized using machine learning were the amplitudes and frequencies of the initial transient stimulation. At  $t=0$ , the oscillatory stimulation is applied and continued until  $t=100$ . The full pattern is formed at  $t=1000$ . The profile at an intermediate timepoint of  $t=800$  is also shown. Lighter shades represent cells depolarized potentials of about -5 mV and darker shades correspond to hyperpolarized potentials of about -55 mV. Red arrows indicate force field vectors at the field grid points.

	Stigmergic model	Mosaic model
$\widehat{MI}(\text{Boundary}; \text{Bulk})$	$0.716 \pm 0.001$	$0.2108 \pm 0.0003$
$\widehat{CS}(\text{Boundary}, \text{Bulk})$	$0.828 \pm 0.009$	$0.4689 \pm 0.0009$
$\Delta D$	$44.5\% \pm 0.8\%$	0%
RFC	6.6%	2.5%

Table 1. Metrics showing the degree of bulk-boundary interactions, along with RFC, present in the stigmergic and mosaic models.

### The stigmergic patterning model fortuitously recapitulated key qualitative features of *Xenopus* bioelectric facial prepatter development

Do the minimal vertebrate face patterning models described above have anything to say about bioelectric prepatter development observed in real embryos? We compared patterns from various stages of our models and actual *Xenopus* embryos [30] and found that the stigmergic model indeed displayed qualitative resemblance to some of the key features

of the developmental sequence of the craniofacial bioelectric prepatter observed in the embryo (Figure 9).

The *Xenopus* craniofacial bioelectric prepatter development goes through several stages but we focus on the following features. The patterning sets off with a broad hyperpolarized region appearing in the anterior central portion stretching down the middle of the future face (yellow arrow in Figure 9A), later thinning out (purple arrow in Figure 9B) and splitting into features representing the future nose and the mouth (green arrows in Figure 9C). This is followed by the inception of a “ring of fire” that spreads in the form of semicircles around the left and right edges of the face (red arrows in Figure 9D), at the same time lighting up the region of the future left eye (Figure 9E). These regionalization events are spatially but not temporally matched by the patterning sequence displayed by the stigmergic model. Specifically, the initiation of the sequence with the formation of the broadly hyperpolarized nose region of Figure 9A is matched by a similar initiation in our model (yellow arrow in Figure 9a), with its later thinning out and splitting into two also matched by our model (purple and green arrows in Figures 9b, 9c). Furthermore, the formation of the “ring of fire” with the concomitant lighting up of the eye region are also matched by our model (Figures 9b, 9c). Nonetheless, the timing of these events are not precisely matched. In particular, the ring of fire and eye formation follow the nose-mouth splitting event in reality, whereas they happen in parallel in our model (red arrows appear throughout).

Differences aside, the similarities are indeed striking and suggest the possibility that general principles of bioelectric patterning may exist in embryogenesis, especially since we didn’t design the model to match observed data nor did we optimize it to develop the

patterns in a specific sequence. In particular, it suggests that morphogenesis may be strongly constrained even by the relatively simple assumptions of our model.

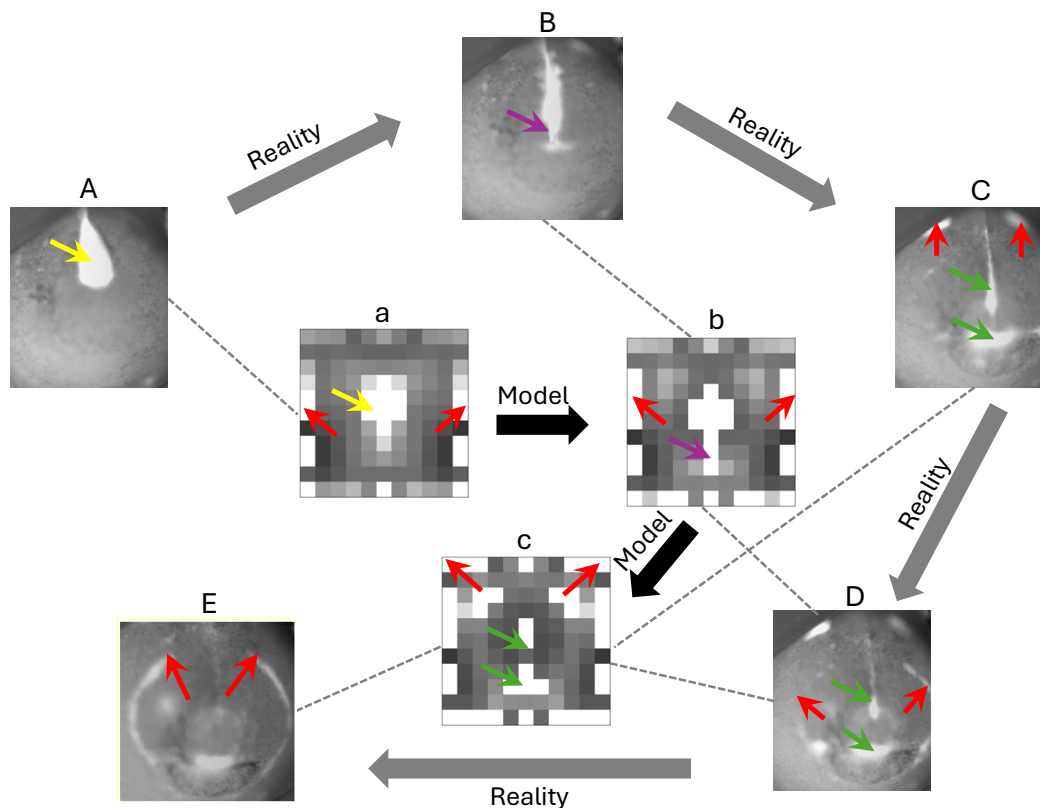


*Figure 9.* Comparison between the pattern sequence of the stigmergic model and the actual sequence of bioelectric prepatterning development observed in frog embryos. The inner sequence connected by thick black arrows represents the model and the outer sequence connected by thick grey arrows represents empirical data. Colored arrows in each image represent specific patterning events. Matching colors in model versus reality indicate matching events. The black dashed lines connecting pairs of model and empirical images indicate the existence of at least one matching event.

## Methods

### Model details

The bioelectric field model is a two-dimensional multicellular network where the cells consist of simplified bioelectric circuits, are structurally connected via gap junctions with a topographic (lattice) connectivity and are endowed with an electrostatic force field by virtue of their charge content or equivalently  $V_{\text{mem}}$  (Figure 9). The core bioelectric model, consisting of the cells equipped with a pair of generic voltage-gated polarizing and depolarizing ion channels and voltage-gated gap junctional intercellular connectivity was adopted from Refs [69,116]; no extracellular medium is assumed in this model. For the model used in this paper, the conductance of the depolarizing channel,  $G_d$ , was set to a fixed value of 1.5 nS (nano Siemens) but modulated by a factor proportional to the difference between the  $V_{\text{mem}}$  of the equilibrium potential of the depolarizing channel  $E_d$ . While the conductance of the polarizing channel,  $G_p$ , was voltage-gated in an analogous way, it was also subject to further modulation by the electric field in a qualitatively similar way as

voltage-gating (Figure 9). The joint action of the ion channels endow the cell with bistability, allowing the  $V_{\text{mem}}$  to converge to one of two values, namely -5 mV and -55 mV separated by an unstable equilibrium at -9 mV [69]. The gap junctions were gated in such a way that it is most conductive when the  $V_{\text{mem}}$  of the cells it connects are the same and least conductive when the difference is the most, allowing the tissue to spatial regionalization [69].

The above core bioelectric model was further furnished with an electric field as follows. The 2D cellular lattice is enmeshed by a separate 2D “field lattice”: the cells are interspersed with “field grid points” (small grey circles in Figure 9) where the fields emitted from cells throughout the tissue aggregate (solid red arrows in Figure 9) and regulate the bioelectric state of nearby cells. Though in reality every conceivable point in the intercellular space would constitute the field, we adopted the simplest approximation of it where each cell is surrounded by just four grid points under the assumption that such a configuration most optimally captures the spatial relationship between the field and the cells. Thus, if the lattice dimensions of the cellular network are  $r \times c$ , with the total number of cells equal to  $n_c = r * c$ , then the total number of field grid points would be equal to  $n_f = (r + 1) * (c + 1)$ . The force vectors at each field grid point are computed and added as per Coulomb’s law of electrostatics, where the charge content of a cell was calculated using its  $V_{\text{mem}}$  and membrane capacitance. We additionally assumed that the relative permittivity of the cytoplasm set to  $10^7$  [147-149]. Even though, in principle, every cell could contribute to the net force at every field grid point, we allow the range of influence termed as the “field action range” to vary as a parameter of the model ( $R$ ) in order to accommodate the effects of “field screening” [111](red dashed arrows in Figure 9). Specifically, only those cells within a distance of  $\sqrt{2}rR$  from a field grid point can influence it. Thus, if  $R = 1$  only the immediately neighboring cells influence a grid point and when  $R = 2m - 1$ , where  $m$  is the larger of the two lattice dimensions then the whole tissue influences it.

The transduction mechanism by which the electric field around a cell regulates its bioelectric state works as follows. When the average magnitude of the force vectors (black dashed arrows in Figure 9), after being transformed by a weighted ( $W$ ) sigmoid, exceeds a threshold  $B$  the  $G_p$  of the contained cell decreases resulting in its gradual depolarization; below the threshold,  $G_p$  increases, resulting in hyperpolarization. Thus, when  $B = 0$  all the cells depolarize and when  $B = \infty$  the entire tissue hyperpolarizes. For intermediate values of  $B$ , heterogenous mixtures of states can appear, with a typical convergent pattern characterized by a set of hyperpolarized cells at the center of the tissue surrounded by depolarized cells (Figure 3). This symmetry can however be broken by choosing a high  $W$ , low  $B$  and an intermediate value of  $R$  that creates an optimal negative feedback relationship between the field and  $V_{\text{mem}}$ , resulting in a continuous generation of novel patterns (see Supplementary Material Movies S1-S3). In general, complex patterning requires a sufficient degree of sensitivity to changes in the field that can be propagated through the tissue at varying spatiotemporal rates. The transduction parameters that determine the strength of field sensitivity are  $W$  and  $B$ . Accordingly, to better understand the effects of field sensitivity on patterning, we classify the models into two broad categories: *strongly sensitive* (high  $W$  and low  $B > 0$ ) and *weakly sensitive* (low  $W$  and high  $B$ ). The combination of field sensitivity

strength and  $R$  result in different types of patterns with varying degrees and spatial configuration of contrast, examples of which are shown in Figure 3.

$$C \frac{dv_i}{dt} = -\frac{G_{p_i}(v_i - E_p)}{1 + e^{\frac{z(v_i - v_{th})}{v_T}}} - \frac{G_{d_i}(v_i - E_d)}{1 + e^{\frac{z(v_i - v_{th})}{v_T}}} + \sum_{j \in N_{C_i}} (v_j - v_i) G_{ij}$$

$$G_{ij} = \frac{2GG_r}{1 + \cosh\left(\frac{v_i - v_j}{v_0}\right)}$$

$$G_r \frac{dG_{p_i}}{dt} = -G_{p_i} + 2W \left( \sigma \left( - \sum_{j \in N_{F_i}} \frac{\|\vec{e}_j\|}{|N_{F_i}|} + B \right) - 1 \right)$$

$$\vec{e}_i = \frac{k_e}{\epsilon_r} \sum_j \frac{q_j}{\|\vec{r}_{ji}\|^2} \delta(\vec{r}_{ji} - \sqrt{2}rR)$$

$$q_j = C v_j$$

Where:

$r = 5 \mu m$ , the radius of a cell

$n_c$  = total number of cells

$N_{C_i}$  = the set of neighboring cells of cell  $i$

$n_f$  = total number of field grid points

$N_{F_i}$  = the set of neighboring (within perception range) field grid points of cell  $i$

$v_i = V_{mem}$  of cell  $i$  (Volts)

$\vec{e}_i$  = electric field vector at field grid point  $i$ ;  $\|\vec{e}_i\|$  measured in (Volts/m)

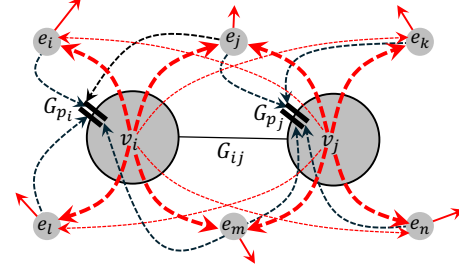
$q_j$  = charge content of cell  $j$  (Coulombs)

$\vec{r}_{ji}$  = distance vector from cell  $j$  to field grid point  $i$

$G_{ij}$  = the conductance of the gap junction connecting cells  $i$  and  $j$  (Siemens)

$G_{p_i} = P * G_r$ ;  $P \in [0.0, 2.0] \in [0.0, 2.0]$ ,

the conductance of the polarizing ion channel of cell  $i$  (Siemens)



$G_{d_i} = 1.5 nS$ , the conductance of the depolarizing ion channel of cell  $i$  (S)

$G_r = 1.0e^{-9} S$ , the reference value for scaling ion channel and gap junction conductance (Siemens)

$C = 0.1e^{-9} F$ , the capacitance of the cell membrane (Farads)

$E_p = -55 mV$ , the equilibrium potential of polarizing channel

$E_d = -5 mV$ , the equilibrium potential of depolarizing channel

$G$  = Gap junction strength  $\in [0.0, 1.0]$  (A. U.)

$R$  = field action range (A. U.)

$W$  = field transduction weight (A.U.)

$B$  = field transduction threshold (Volts/m)

$\sigma(\cdot)$  = sigmoid transformation

$\delta(\vec{r}_{ji} - d)$  = delta function with value 1 when  $\|\vec{r}_{ji}\| \leq d$  and 0 otherwise

$k_e = 8.987e^9 Nm^2 C^{-2}$ , the Coulomb electric field constant

$\epsilon_r = 10^7$ , the presumed relative permittivity of cytoplasm

**Figure 10.** Mathematical description of the model with a mapping illustration of a two-cell version of the model shown for clarity. Red arrows in the illustration indicate force field vectors at field grid points. The red dashed lines indicate the electric field lines, with their weights representing the magnitude of field strength. The black dashed lines connecting field grid points with the ion channels represent field transduction.

## Model simulation

The initial conditions of the variables in each simulation were set as follows:  $v = -9.2$  mV and  $\vec{e} = 0$  V/m for all cells;  $G_d = 1.5G_r$  for all cells;  $G_p = P * G_r$  where  $P$  was randomly chosen from the range  $[0.0, 2.0]$  for each cell in simulations with heterogenous initial conditions, and set to a constant value of 1.0 for all cells in simulations with homogenous initial conditions;  $G_0 = G * G_r$ ;  $G \in [0.0, 1.0]$  in all simulations except for the face patterning models where  $G$  was set to 0.05;  $R$  was varied in the range  $[1, 21]$  in all simulations except for the face patterning models where it was set to 4;  $W$  was varied in the range  $[10, 1000]$  in all simulations except for the face patterning models where it was set to 10 for the mosaic model and 1000 for the stigmergic model;  $B$  was varied in the range  $[0.0005, 0.02]$  in all simulations except for the face patterning models where it was set to 0.02 for the mosaic model and 0.0005 for the stigmergic model. The model equations were integrated using the standard Euler method with a fixed step size of 0.01 for about  $T$  steps where  $T$  was varied between 500 and 5000 depending on the experiment.

## Model analysis measures

The Tononi-Edelman-Sporns (TSE) measure of complexity is a measure of the balance between integration and segregation contained in a dynamical system. It is defined as the sum of mutual information between all possible subsets of a system and their respective complements (bipartitions) of a system [130], mathematically expressed as:

$$TSE(X) = \sum_{k=1}^{n/2} \langle MI(X_j^k; X - X_j^k) \rangle$$

It is equivalently stated as:

$$TSE(X) = \sum_{k=1}^{n/2} [\langle H(X_j^k) \rangle - (k/n)H(X)]$$

Here,  $X$  refers to the system containing  $n$  elements, and  $X_j^k$  refers to the  $j^{th}$  subset of size  $k$ . The operator  $\langle . \rangle$  refers to the average taken over all possible  $n!/(k!(n-k)!)$  combinations of subsets containing  $k$  elements. The terms  $MI(.)$  and  $H(.)$  refer to mutual information and Shannon entropy respectively [150]. TSE becomes zero in fully segregated systems where the joint entropy of the system  $H(X)$  is equal to the sum of the entropies of its elements and in fully integrated systems where the joint entropies of subsets are simply scaled versions of the whole. Here we considered random samples of subsets due to the exponentially large number of combinations of partitions for a system containing 121 elements (cells). Specifically, we considered 50 equally spaced partition sizes in the range [2,120], and for each partition size we considered 100 randomly samples subsets. We used the *Python* package *dit* (short for discrete information theory [151]) for computing  $MI$  and  $H$ . Since they are designed for binary data, we binarized all of the  $V_{mem}$  timeseries generated by our model by assigning a value of 0 to  $V_{mem}$  in the range [-40 mV, 0 mV] and a value of 1 to  $V_{mem}$  values in the range [-80 mV, -40 mV). We chose these ranges by observing that the  $V_{mem}$  values generated by our simulations typically varied within the range [-80 mV, 0 mV].

“Relative field compression” (RFC) is a measure of the ratio of the dimensionality of the field to the dimensionality of  $V_{mem}$  of the tissue. We defined the dimensionality of a variable as the total variance explained by its first three PCA dimensions. Specifically, if we denote the percentage variance explained by the first three PCA dimensions of the  $V_{mem}$  timeseries as  $p_1^v, p_2^v$  and  $p_3^v$ , and the corresponding terms of the field as  $p_1^e, p_2^e$  and  $p_3^e$  then RFC is defined as:

$$RFC = (p_1^e + p_2^e + p_3^e) - (p_1^v + p_2^v + p_3^v)$$

“Field influence” (FI) is a measure of the sensitivity of  $V_{mem}$  to the field, defined as the mean rate of change of  $V_{mem}$  of a target cell at every step of the simulation with respect to small changes in the electrostatic force of source field grid points at the beginning of the simulation averaged over all source-target combinations and time:

$$FI = \frac{\sum_{\tau=1}^T \sum_{j=1}^{n_f} \sum_{i=1}^{n_c} \left| \frac{\partial v_i(t=\tau)}{\partial e_j(t=0)} \right|}{T * n_c * n_f}$$

Causal strength (CS) is a measure of the strength of interaction among the cells that we first introduced in [152]. It is defined as the mean rate of change of  $V_{mem}$  of target cells at every step of the simulation with respect to small changes in the  $V_{mem}$  of source cells at the beginning of the simulation averaged over all source-target combinations and time:

$$CS = \frac{\sum_{i=1}^{n_c} CS(i)}{n_c}$$

where:

$$CS(i) = \frac{\sum_{j=1}^{n_c} CS(i, j)}{n_c}$$

where:

$$CS(i, j) = \frac{\sum_{\tau=1}^T CS(i, j, \tau)}{T}$$

where:

$$CS(i, j, \tau) = \left| \frac{\partial v_i(t = \tau)}{\partial v_j(t = 0)} \right|$$

Causal distance (CD) is a measure of the distance of the most causally influential variables in a system, defined as the mean distance of the top 5 cells in terms of their causal strength averaged over all cells:

$$CD = \frac{\sum_{i=1}^{n_c} CD(i)}{n_c}$$

where:

$$CD(i) = \frac{\sum_{j \in \text{top } 5 \{CS(i, j)\}} d(i, j)}{n_c}$$

where,  $d(i, j)$  represents the Euclidean distance between cells  $i$  and  $j$ .

For figures 4-6 we estimated  $FI$ ,  $CS$  and  $CD$  rather than compute them exactly for practical reasons by choosing 50 equally spaced points in the range  $[1, T]$ ; and by choosing three representative target cells with locations (0,0), (0,6) and (6,6) in the 11x11 lattice, representing the cells at the corner, middle of the boundary and center of the tissue respectively, thereby spanning the extremities of the tissue's topography.

The normalized mutual information between the bulk and the boundary,  $\widehat{MI}(Bo; Bu)$ , is a measure of the proportion of correlation between the bulk and the boundary with respect to the expected correlation between partitions of similar sizes. It is defined as the ratio of MI between the bulk and the boundary and the expected MI between any bipartition of the system where one partition is the same as the boundary and its complement naturally the size of the bulk:

$$\widehat{MI}(Bo; Bu) = \frac{MI(Bo; Bu)}{\langle MI(X_j^{|Bo|}; X - X_j^{|Bo|}) \rangle}$$

Here the set of indices corresponding to the bulk is denoted as  $\{Bu\}$ , the set of indices corresponding to the boundary  $\{Bo\}$ , the set of indices corresponding to a partition the size of the boundary as  $\{X_j^{|Bo|}\}$  and its complement as  $\{X - X_j^{|Bo|}\}$ , with  $j$  referring to the index of a single partition. To estimate  $\widehat{MI}(Bo; Bu)$ , we randomly sampled 100 bipartitions from a possible  $n!/(|Bo|!(n - |Bo|)!)$  number of bipartitions.

The normalized causal strength between the boundary and the bulk,  $\widehat{CS}(Bu, Bo)$ , is a measure of the proportion of the causal strength between the boundary and the bulk with respect to the expected causal strengths between partitions of similar sizes at a given instant of time, averaged over all time points. The notations follow the same conventions as above. As before, we estimated  $\widehat{CS}(Bu, Bo)$ , by randomly sampling 100 bipartitions from a possible  $n!/(|Bo|!(n - |Bo|)!)$  number of bipartitions as well as by sampling  $\tau$  by choosing 50 equally spaced points in the range  $[1, T]$ ;

$$\widehat{CS}(Bu, Bo) = \frac{\sum_{\tau=1}^T \frac{\sum_{i \in \{Bu\}} \sum_{j \in \{Bo\}} CS(i, j, \tau)}{\langle \sum_{i \in \{X - X_j^{|Bo|\}} \sum_{j \in \{X_j^{|Bo|\}} CS(i, j, \tau) \rangle}}}{T}$$

Finally,  $\Delta D$  is a measure of deformity in the output pattern caused due to differences in the past boundary states. Specifically, let  $D$  be the Euclidean distance between the observed pattern at the end of 1000 simulation steps and the target vertebrate face pattern. Let  $D'$  be the Euclidean distance between the observed pattern at the end of 1000 simulation steps following a transient perturbation and the target vertebrate face pattern. The perturbation was at the end of the stimulation period (first 100 steps), when the  $G_p$  values of the cells at the boundary of the tissue (44 cells in the 11x11 lattice) were randomly permuted. To compute the variation of the measure we ran a set of 100 simulations each consisting of a unique permutation of the boundary states.

### Model optimization

We used machine learning techniques to optimize the oscillatory stimulation values of the model required for generating a vertebrate face pattern (the model parameters were fixed). The stimulation was applied on a set of 44 field grid points located on the boundary of the tissue (Figures 7 and 8). However, since the target is bilaterally symmetrical (about the vertical bisection axis) the stimulation values of only 22 points had to be learned, with the other being a mirror reflection of the former. The stimulation values associated with each of those points consisted of the amplitude, phase and frequency of the corresponding oscillatory voltage input. The initial ranges associated with the variables set at the beginning of the optimization were as follows: [100 mV, 500 mV] for the absolute value of the amplitude;  $[0, 2\pi]$  for the phases; and [100 Hz, 1000 Hz] for the frequency. The learned values of the amplitudes and frequencies were allowed step out of those initial ranges but the phase was limited to the initial range. The stimulation period was set to the first 10% of the duration of simulation during which the stimulated points were clamped with the corresponding input voltage trains and the resulting force field vectors were computed at all the other field grid points. We treated the stimulated field grid points as cells, so their “charges” were computed using the applied voltage and the membrane capacitance of a cell. As for the specifics of the machine learning algorithm, we used gradient descent, a method that updates the parameters to be learned by taking a small step in the direction of the steepest descent where the height of the parameter landscape represents performance (deeper points are better) [146]. Here we used a specific form of gradient descent method known as “resilient backpropagation” [153], which relies only on the sign (not the magnitude) of the gradients



for updating the parameters at every iteration. For the cost function (performance), we used the root mean squared distance between the observed patterns during the last 10% of the simulation and the target face pattern.

## **Discussion**

Our goal was to understand the role of a continuous (fluid) electrostatic force field in the dynamic behavior of a discrete (solid) non-neural multicellular bioelectric network that it permeates. Our investigations revealed that the field indeed enhances the patterning capabilities of the network, as evidenced by its ability to regulate the pattern complexity, dimensionality and causal catalysis of the spatial  $V_{\text{mem}}$  states. Our results support the hypothesis that the field regulates  $V_{\text{mem}}$  patterning by effectively turning into a control parameter by virtue of its lower dimensionality and slower timescale compared to the spatial  $V_{\text{mem}}$  state, despite the circular feedback between them, in a manner consistent with a principle of synergetics in which fast variables are controlled by slow variables that effectively act as control parameters [133]. We leveraged these results to prime the system to develop specific target patterns simply by transiently stimulating the field surrounding the boundary of the tissue. We used machine learning, specifically automatic differentiation based gradient descent, to learn the oscillatory stimulation sequence and optimize a pair of models with opposite field sensitivity strengths to generate a vertebrate face pattern. An analysis of those models revealed that they developed the face patterns using very different strategies, namely, a mosaic and stigmergy based mechanism depending on whether the field sensitivity strength was weak or strong respectively. In summary, our work suggests that the electrostatic field could indeed function as a key facilitator of voltage patterning in embryonic tissues, thereby contributing to morphogenetic pre-patterning processes in real biological systems. We interpret our results to further suggest that the electric field also can have the potential to act as a top-down control knob that when tuned appropriately could steer a real or synthetic biological system employing bioelectricity to generate desired patterns.

### **Implications for morphogenesis**

The field concept was originally proposed in the early twentieth century as a response to the prevailing view at the time of predeterminism or “preformism” as explicated in Wilhelm Roux’s “mosaic theory of development” that later became synonymous with genetic determinism [11,14,154]. Proponents of the field concept argued that the properties of the whole could not be deduced from the individual parts and that it is the relational organization of the system that was key. This view was supported by Hans Driesch’s groundbreaking embryo-cutting experiments [13] that essentially showed that the developmental fate of the cells in an embryo should be attributed not only to their genetic states but also to their spatial locations in the tissue [10]. Thus, the concept of positional information was born and along with it the general concept of the morphogenetic field that expressed informational and regional relationships [15], the prototypical example of which is the morphogen gradient or the “French flag” model as is popularly known [16]. Besides the conventional sources of

positional information, such as biochemical and transcriptional gradients, patterns of bioelectric potentials can also provide such information to the cells for appropriate differentiation during development [15,155].

Here we found that adding a true field dynamic to a bioelectric patterning system can enhance its capacity for emergent self-organization of morphogenetic prepatterns. Given that prepatterning and positional information are deeply connected [18,156], this result has implications for the developmental biology as it suggests that a bioelectric *field* basis of morphogenesis is viable. Our model serves as a concrete example that illustrates several ideas and hypotheses on the role of the field in morphogenesis that were articulated in the early twentieth century. For instance, Alexander Gurwitsch found that describing the outlines of an embryo is simpler than describing the details of its parts, a function that he proposed was carried by some kind of field [13]. He moreover proposed that such a field was constituted by the developing body itself that in turn was shaped and refined by the field, an idea that was shared by Harold Burr as well [13]. Our model shows that the electrostatic field could serve the role of the hypothetical field described in the early ideas, as it shares some of the requisite properties of the field stated above. For instance, if we take any of the force field profiles shown in Figure 7 or 8 and remove all the cells, leaving only the force vectors in place, then one would see the outline of the face and not its parts. This picture would become even more coarse-grained if one were to average those vectors with discrete segments of the picture. This “blurring” property of the field is also compatible with its lower dimensionality (Figure 5), as coarse-graining loses (redundant) information, a property that supports Gurwitsch’s idea that it’s simpler to describe outlines than the details of an embryo.

Our work goes further and shows that there may be more complex strategies for developing prepatterns than what is known such as ‘French flag’ model [16], the ‘clock and wavefront’ model [157] and even the somewhat complex hierarchical patterning models [158]. Specifically, we show that it is possible to generate complex patterns by leveraging stigmergic strategies that neither requires significant incipient information such as the French flag model nor mechanisms of gradual complexification such as the hierarchical model. Moreover, our finding that the stigmergic model required stimulation at biologically plausible ranges (order of millivolts) suggests that evolution could exploit such a system for endogenous control of morphogenesis. A related phenomenon has been suggested to occur in early patterning of the left-right axis where cells on the ventral midline generate a bioelectric gradient which then impacts the axial identity of cells throughout the body by driving re-distribution of small molecule morphogens (likely serotonin) across the embryonic field [35,159-161].

#### Ephaptic coupling and long distance communication

Neuronal cells have long been known to communicate not only through synaptic coupling but also via electric field interactions known as “ephaptic coupling” [162]. These interactions happen without any physical connectivity (the term “ephaptic” means “touching”), and therefore they are often considered to be less pronounced compared to other conventional means [162]. However, recent research has begun to unravel the potential effects ephaptic coupling may have on a wide range of neural phenomena such as

memory, cognition and even consciousness [99,100,102,126,163]. This has led to proposals for including ephaptic coupling in modeling efforts, especially given the differential propagation speed it offers over synaptic and biochemical routes [164] thus enabling a Turing-like setting to facilitate patterning and development [165]. Our work is most closely related to recent research that showcased the role of the electric field in establishing and maintaining memory engrams by virtue of its lower dimensionality and higher stability compared to neuronal activity [99-101]. Our minimal model exemplifies these ideas in a non-neural setting (embryonic patterning), thereby demonstrating the potential substrate-free ability of the electric field to regulate disparate phenomena.

Electric field mediated ephaptic coupling has the potential to facilitate long-distance communication that has been hypothesized, and robustly demonstrated in some cases, to play important roles in developmental phenomena such as neurulation, pigmentation, morphogenetic patterning, craniofacial development, body axis establishment and even cancer [135]. Moreover, long-distance communication facilitates the diagnosis as well as treatment of injuries at a location that is spatially separated from the source [69,166]. Our model serves as a minimal but concrete example demonstrating how long-distance communication (controlled by the field range parameter) could facilitate morphogenetic patterning and potentially in other aspects of development. Additionally, unlike other models of long-distance communication [69,167,168] as well as reaction-diffusion based patterning models [158,169], our model possesses a unique “hopping” property where an activity source triggers distant parts of the tissue without setting off the cells enroute (Figure 8). The bioelectric face patterning in *Xenopus* embryos indeed displays such characteristics (though it is not yet clear that they are causal) and there may be several other phenomena in development with hopping characteristics requiring field-based explanations.

### Limitations of the current study

In this work we developed and analyzed a minimal bioelectric field model of morphogenetic patterning. Though we learnt several properties of this model it has certain limitations that may prohibit us from extrapolating the results to real biological systems. First, our model does not simulate the extracellular medium that could play a role in morphogenesis by providing structural support, a medium for transmitting biochemical signals and affecting a wide range of behaviors including cell polarity, adhesion and migration [170]. The extracellular medium may contain charged particles that may limit the penetration of the electric field into the tissue due to a phenomenon known as “charge screening” [111]. Even though we partially address this issue by parameterizing the reach of the field real biological tissues may possess additional complexities that might limit the role of the electric field in patterning processes.

As our goal was to understand the phenomenological effects of including a true field in a dynamical system, and not the physiological effects, we did not assume biophysically realistic parameters in the model. For instance, we assumed the relative permittivity of the cell as  $10^7$ , a value we adopted from a wide range of values reported in the literature ranging from a frequency-dependent value of 60 reported in Refs [171-173] to static permittivity values ranging in  $10^4$  to  $10^7$  as reported in Refs [147-149]. Even though choice of this value could significantly alter the results, it is possible that it could be compensated by another

unknown mechanism thus preserving the broad character of our results. Lastly, we have not included gene regulatory networks and a plethora of other biomolecular factors that could in theory weaken or strengthen the modulatory effects of the field in vivo.

### Biomedical applications and future directions

The regulatory role and therapeutic potential of bioelectricity during development and regeneration has been demonstrated in numerous vertebrate and invertebrate models (reviewed in [174]). The work on the *Xenopus* bioelectric face patterning, for instance, has shown that disrupting the bioelectric pattern leads to craniofacial abnormalities [30], while introducing components of the native electric face pattern into other regions induces the formation of complex ectopic organs such as eye [36].

Moreover, targeted repair of the pattern can rescue defects induced by teratogens or mutations [68,70,175,176]. Work in frog, flatworm, and *Drosophila* models have implicated bioelectric prepatterns as instructive influences over gene expression and subsequent anatomy. Future exploitation of this interface for therapeutic purposes requires the ability to impose desired complex patterns on tissues, and to understand what kinds of influences could disrupt the processes of morphogenesis in the context of birth defects and failures to regenerate after damage. Having established several qualitative similarities with the observed real developmental sequence (Figure 9), our stigmergic model made a new prediction that disrupting the bioelectric state of the *boundary* alone could also result in craniofacial abnormalities of tissues inside it. This prediction along with the result that the most causally influential cells are not the spatially closest ones, especially in optimal patterning models (Figure 6), suggests that the field may better facilitate therapeutic and biomedical interventions by providing alternatives to invasive procedures. Moreover, we found that the strongest causal influence does not necessarily stem from the nearest cells but sometimes emanates from cells further away. This may have implications for surrogate site diagnostics and interventions on deep tissues that exert their influence from a more easily-accessed location. We plan to test these hypotheses in future experimental work.

Predicting downstream outcomes by intervening into upstream processes constitutes what is known as the “forward problem” [177]. There is another much harder to solve class of problems known as the “inverse problem” where the goal is to find upstream states given downstream states [177,178]. It is known that linear encodings of morphology, such as fate maps and prepatterns, are easier to derive for given desired target morphologies due to the property called “invertibility”, something that nonlinear encodings such as gene expression patterns do not possess making them notoriously difficult to solve [178]. By leveraging machine learning techniques, especially automatic differentiation based gradient descent, our work offers a potential solution to the inverse problem by inferring encodings (initial conditions) in a field-based dynamical model of morphogenesis that would temporally unfold and decode into the associated target patterns. It is noteworthy that the method underlying our approach has been famously used for the optimization of neural network inputs (not model parameters) to generate hallucinatory images in computer programs such as Google’s ‘deep dream’ [179]. In future work we plan to exploit this technological capability to guide the patterning of real and synthetic biological systems.

Traditional electrode applications make it very difficult to induce predictable, complex patterns of stable resting potentials in non-excitable cells. However, our model suggests that taking the field into account, it may be possible to design stimulation that results in desired bioelectric distributions in tissue. If this bears out in vivo, it would be a significant addition to the current toolbox of electroceuticals and wearable bioreactors [180,181] addressing birth defects, regeneration, cancer reprogramming [26,61] and the bioengineering of multicellular living constructs [182-185].

## Acknowledgements

We thank Patrick McMillen for helpful comments on the manuscript. We gratefully acknowledge funding from the Emerald Gate Trust.

## Author Contributions

M.L. and S.M. conceptualized the work. S.M. wrote code and conducted the computational experiments. M.L. and S.M. analyzed and interpreted the data, and wrote the manuscript.

## References

- [1] K. D. Birnbaum and A. S. Alvarado, *Cell* **132**, 697 (2008).
- [2] A. K. Harris, *Biosystems* **173**, 65 (2018).
- [3] M. Levin, *Regenerative medicine* **6**, 667 (2011).
- [4] D. E. Ingber and M. Levin, *Development* **134**, 2541 (2007).
- [5] B. C. Goodwin and L. E. Trainor, *J Theor Biol* **85**, 757 (1980).
- [6] V. French, P. J. Bryant, and S. V. Bryant, *Science* **193**, 969 (1976).
- [7] W. A. M. Brandts and L. E. H. Trainor, *Journal of Theoretical Biology* **146**, 57 (1990).
- [8] W. A. M. Brandts and L. E. H. Trainor, *Journal of Theoretical Biology* **146**, 37 (1990).
- [9] Y. Schiffmann, *Prog Biophys Mol Biol* **89**, 36 (2005).
- [10] H. S. Burr and F. S. C. Northrop, *The Quarterly Review of Biology* **10**, 322 (1935).
- [11] H. S. Burr, *The Scientific Monthly* **64**, 217 (1947).
- [12] H. Margenau, *The Scientific Monthly* **64**, 225 (1947).
- [13] M. Bischof, in *Biophotons* (Springer, 1998), pp. 375.
- [14] A. Tzambazakis, *Fields of the Cell. Research Signpost*, 1 (2015).
- [15] M. Levin, *Biosystems* **109**, 243 (2012).
- [16] L. Wolpert, *Journal of theoretical biology* **25**, 1 (1969).
- [17] A. M. Turing, *Philos T Roy Soc B* **237**, 37 (1952).
- [18] S. T. Vittadello, T. Leyshon, D. Schnoerr, and M. P. H. Stumpf, *Philos Trans A Math Phys Eng Sci* **379**, 20200272 (2021).
- [19] T. Leyshon, E. Tonello, D. Schnoerr, H. Siebert, and M. P. H. Stumpf, *J Theor Biol* **531**, 110901 (2021).
- [20] Y. Schiffmann, *Prog Biophys Mol Biol* **105**, 258 (2011).
- [21] Y. Schiffmann, *Progress in biophysics and molecular biology* **98**, 107 (2008).

- [22] M. L. Steyn-Ross, D. A. Steyn-Ross, M. T. Wilson, and J. W. Sleight, Physical review. E, Statistical, nonlinear, and soft matter physics **76**, 011916 (2007).
- [23] Y. Schiffmann, Progress in biophysics and molecular biology **56**, 79 (1991).
- [24] R. H. W. Funk and F. Scholkmann, Prog Biophys Mol Biol **177**, 185 (2023).
- [25] R. Funk, Biological Systems (2013).
- [26] M. Levin, Cell **184**, 1971 (2021).
- [27] E. Bates, Annu Rev Cell Dev Biol **31**, 231 (2015).
- [28] M. P. Harris, Development **148** (2021).
- [29] D. S. Adams, S. G. Uzel, J. Akagi, D. Wlodkowic, V. Andreeva, P. C. Yelick, A. Devitt-Lee, J. F. Pare, and M. Levin, J Physiol **594**, 3245 (2016).
- [30] L. N. Vandenberg, R. D. Morrie, and D. S. Adams, Dev Dyn **240**, 1889 (2011).
- [31] W. S. Beane, J. Morokuma, D. S. Adams, and M. Levin, Chemistry & Biology **18**, 77 (2011).
- [32] F. Durant, J. Bischof, C. Fields, J. Morokuma, J. LaPalme, A. Hoi, and M. Levin, Biophys J **116**, 948 (2019).
- [33] C. D. Stern, Experimental Cell Research **140**, 468 (1982).
- [34] M. Levin, T. Thorlin, K. R. Robinson, T. Nogi, and M. Mercola, Cell **111**, 77 (2002).
- [35] D. S. Adams, K. R. Robinson, T. Fukumoto, S. Yuan, R. C. Albertson, P. Yelick, L. Kuo, M. McSweeney, and M. Levin, Development **133**, 1657 (2006).
- [36] V. P. Pai, S. Aw, T. Shomrat, J. M. Lemire, and M. Levin, Development **139**, 313 (2012).
- [37] R. J. Nuckels, A. Ng, T. Darland, and J. M. Gross, Invest Ophthalmol Vis Sci **50**, 893 (2009).
- [38] S. K. Schotthofer and J. Bohrmann, BMC Dev Biol **20**, 15 (2020).
- [39] I. Weiss and J. Bohrmann, BMC Dev Biol **19**, 22 (2019).
- [40] I. Weiss and J. Bohrmann, BMC Developmental Biology **19**, 12 (2019).
- [41] R. I. Woodruff and W. H. Telfer, J Cell Biol **58**, 172 (1973).
- [42] W. H. Telfer and R. I. Woodruff, J Insect Physiol **48**, 915 (2002).
- [43] T.-X. Jiang *et al.*, iScience **24**, 102671 (2021).
- [44] M. R. Silic and G. Zhang, Cells **12** (2023).
- [45] C. Yi *et al.*, Elife **10** (2021).
- [46] S. Kujawski *et al.*, Dev Cell **28**, 573 (2014).
- [47] S. Perathoner, J. M. Daane, U. Henrion, G. Seeböhm, C. W. Higdon, S. L. Johnson, C. Nusslein-Volhard, and M. P. Harris, PLoS genetics **10**, e1004080 (2014).
- [48] M. T. Belus, M. A. Rogers, A. Elzubeir, M. Josey, S. Rose, V. Andreeva, P. C. Yelick, and E. A. Bates, Dev Biol **444 Suppl 1**, S297 (2018).
- [49] V. P. Pai, C. J. Martyniuk, K. Echeverri, S. Sundelacruz, D. L. Kaplan, and M. Levin, Regeneration (Oxf) **3**, 3 (2016).
- [50] B. T. Chernet and M. Levin, Disease models & mechanisms **6**, 595 (2013).
- [51] S. Sundelacruz, M. Levin, and D. L. Kaplan, Stem Cell Rev Rep **5**, 231 (2009).
- [52] D. J. Blackiston, K. A. McLaughlin, and M. Levin, Cell Cycle **8**, 3519 (2009).
- [53] Y. Zhou *et al.*, Science **349**, 873 (2015).
- [54] M. Levin and C. J. Martyniuk, Biosystems **164**, 76 (2018).
- [55] A. Tseng and M. Levin, Communicative & Integrative Biology **6**, 1 (2013).

- [56] A. S. Tseng, W. S. Beane, J. M. Lemire, A. Masi, and M. Levin, *J Neurosci* **30**, 13192 (2010).
- [57] B. T. Chernet, D. S. Adams, M. Lobikin, and M. Levin, *Oncotarget* **7**, 19575 (2016).
- [58] S. Zhao, A. S. Mehta, and M. Zhao, *Cell Mol Life Sci* **77**, 2681 (2020).
- [59] B. Reid and M. Zhao, *Adv Wound Care (New Rochelle)* **3**, 184 (2014).
- [60] M. Zhao, L. Chalmers, L. Cao, A. C. Vieira, M. Mannis, and B. Reid, *Progress in retinal and eye research* **31**, 65 (2012).
- [61] S. Balasubramanian, D. A. Weston, M. Levin, and D. C. C. Davidian, *Trends Pharmacol Sci* **45**, 391 (2024).
- [62] P. Sanjuan-Alberte and F. J. Rawson, *Ther Deliv* **10**, 139 (2019).
- [63] M. Levin, J. Selberg, and M. Rolandi, *iScience* **22**, 519 (2019).
- [64] M. Levin, *Wiley Interdisciplinary Reviews: Systems Biology and Medicine* **5**, 657 (2013).
- [65] M. Levin, *The Journal of Physiology* **592**, 2295 (2014).
- [66] K. G. Sullivan, M. Emmons-Bell, and M. Levin, *Commun Integr Biol* **9**, e1192733 (2016).
- [67] M. Emmons-Bell *et al.*, *Int J Mol Sci* **16**, 27865 (2015).
- [68] V. P. Pai and M. Levin, *Wound Repair Regen* (2022).
- [69] V. P. Pai, J. Cervera, S. Mafe, V. Willocq, E. K. Lederer, and M. Levin, *Front Cell Neurosci* **14**, 136 (2020).
- [70] V. P. Pai, A. Pietak, V. Willocq, B. Ye, N. Q. Shi, and M. Levin, *Nature Communications* **9**, 998 (2018).
- [71] S. Tabibzadeh and O. R. Brown, *Aging and Cancer* **5**, 3 (2024).
- [72] L. Pio-Lopez and M. Levin, *Drug Discov Today* **28**, 103585 (2023).
- [73] K. Famm, B. Litt, K. J. Tracey, E. S. Boyden, and M. Slaoui, *Nature* **496**, 159 (2013).
- [74] V. A. Pavlov and K. J. Tracey, *Neuron* **110**, 3627 (2022).
- [75] M. I. Cohen and G. A. Morrill, *Biophysical Journal* **9**, A187 (1969).
- [76] C. D. McCaig, *J Embryol Exp Morphol* **94**, 245 (1986).
- [77] R. B. Borgens and R. Shi, *Developmental Dynamics* **203**, 456 (1995).
- [78] R. Shi and R. B. Borgens, *Dev Dyn* **202**, 101 (1995).
- [79] R. B. Borgens, *Differentiation* **28**, 87 (1984).
- [80] R. Nuccitelli, in *Electromagnetic Fields* 1995), pp. 109.
- [81] R. Nuccitelli, *Curr Top Dev Biol* **58**, 1 (2003).
- [82] K. R. Robinson and C. McCaig, *Annals of the New York Academy of Sciences* **339**, 132 (1980).
- [83] C. D. Cone and M. Tongier, *Oncology* **25**, 168 (1971).
- [84] C. D. Cone, *Journal of Theoretical Biology* **30**, 151 (1971).
- [85] C. D. Cone, Jr., *Oncology* **24**, 438 (1970).
- [86] M. Levin, A. M. Pietak, and J. Bischof, *Semin Cell Dev Biol* **87**, 125 (2018).
- [87] J. Cervera, A. Pietak, M. Levin, and S. Mafe, *Bioelectrochemistry* **123**, 45 (2018).
- [88] A. Pietak and M. Levin, *J R Soc Interface* **14** (2017).
- [89] A. Pietak and M. Levin, *Frontiers in Bioengineering and Biotechnology* **4**, 55 (2016).
- [90] J. Carvalho, *J Theor Biol* **557**, 111338 (2023).

- [91] J. Cervera, P. Ramirez, M. Levin, and S. Mafe, Phys Rev E **102**, 052412 (2020).
- [92] J. Cervera, S. Meseguer, M. Levin, and S. Mafe, Bioelectrochemistry **132**, 107410 (2020).
- [93] J. Cervera, M. Levin, and S. Mafe, The Journal of Physical Chemistry Letters **11**, 3234 (2020).
- [94] H. S. Burr, Proceedings of the National Academy of Sciences of the United States of America **27**, 276 (1941).
- [95] H. S. Burr, Yale Journal of Biology & Medicine **13**, 783 (1941).
- [96] H. S. Burr and F. S. C. Northrop, Proceedings of the National Academy of Sciences of the United States of America **25**, 284 (1939).
- [97] H. S. Burr, *Blueprint for immortality; the electric patterns of life* (N. Spearman, London,, 1972).
- [98] H. S. Burr and F. S. C. Northrop, Quarterly Review of Biology **10**, 322 (1935).
- [99] D. A. Pinotsis and E. K. Miller, Cereb Cortex **33**, 9877 (2023).
- [100] D. A. Pinotsis, G. Fridman, and E. K. Miller, Prog Neurobiol **226**, 102465 (2023).
- [101] D. A. Pinotsis and E. K. Miller, Neuroimage **253**, 119058 (2022).
- [102] C. C. Chiang, R. S. Shivacharan, X. Wei, L. E. Gonzalez-Reyes, and D. M. Durand, J Physiol **597**, 249 (2019).
- [103] C. Qiu, R. S. Shivacharan, M. Zhang, and D. M. Durand, J Neurosci **35**, 15800 (2015).
- [104] C. A. Anastassiou, R. Perin, H. Markram, and C. Koch, Nature neuroscience **14**, 217 (2011).
- [105] C. A. Anastassiou, S. M. Montgomery, M. Barahona, G. Buzsaki, and C. Koch, The Journal of neuroscience : the official journal of the Society for Neuroscience **30**, 1925 (2010).
- [106] M. Kamermans and I. Fahrenfort, Curr Opin Neurobiol **14**, 531 (2004).
- [107] J. G. Jefferys, Physiological reviews **75**, 689 (1995).
- [108] Z. W. Davis, A. Busch, C. Steward, L. Muller, and J. Reynolds, Cell reports **43** (2024).
- [109] E. K. Miller, S. L. Brincat, and J. E. Roy, Current Opinion in Behavioral Sciences **57**, 101388 (2024).
- [110] S. van Bree, D. Levenstein, M. R. Krause, B. Voytek, and R. Gao, PsyArXiv Preprint **10** (2024).
- [111] P. Urone and R. Hinrichs, *College physics* 2016).
- [112] J. Mathews and M. Levin, Dev Neurobiol **77**, 643 (2017).
- [113] N. Palacios-Prado and F. F. Bukauskas, Proc Natl Acad Sci U S A **106**, 14855 (2009).
- [114] F. D. Houghton, Reproduction **129**, 129 (2005).
- [115] J. Cervera, A. Alcaraz, and S. Mafe, J Phys Chem B **118**, 12444 (2014).
- [116] J. Cervera, S. Meseguer, and S. Mafe, Sci Rep **6**, 35201 (2016).
- [117] A. P. Javier Cervera, Michael Levin, Salvador Mafe, Bioelectrochemistry, 45 (2018).
- [118] J. Cervera, S. Meseguer, and S. Mafe, ACS Omega **3**, 13567 (2018).
- [119] J. Cervera, J. A. Manzanares, and S. Mafe, Phys Chem Chem Phys **20**, 9343 (2018).
- [120] S. Manicka and M. Levin, Sci Rep **9**, 18612 (2019).



- [121] S. Manicka, V. P. Pai, and M. Levin, *iScience* **26** (2023).
- [122] S. J. England and D. Robert, *Biological Reviews* **97**, 383 (2022).
- [123] K.-i. Nakajima *et al.*, *Nature communications* **6**, 8532 (2015).
- [124] L. Rems, M. A. Kasimova, I. Testa, and L. Delemotte, *Biophysical journal* **119**, 190 (2020).
- [125] M. Bielfeldt, H. Rebl, K. Peters, K. Sridharan, S. Staehlke, and J. B. Nebe, *Biomedical Materials & Devices* **1**, 146 (2023).
- [126] C. A. Anastassiou, R. Perin, H. Markram, and C. Koch, *Nat Neurosci* **14**, 217 (2011).
- [127] M. D. Petkova, G. Tkacik, W. Bialek, E. F. Wieschaus, and T. Gregor, *Cell* **176**, 844 (2019).
- [128] G. Tkacik and T. Gregor, *Development* **148** (2021).
- [129] M. F. Simsek and E. M. Ozbudak, *Open Biol* **12**, 220224 (2022).
- [130] G. Tononi, O. Sporns, and G. M. Edelman, *Proceedings of the National Academy of Sciences* **91**, 5033 (1994).
- [131] J. T. Francis, B. J. Gluckman, and S. J. Schiff, *Journal of Neuroscience* **23**, 7255 (2003).
- [132] J. C. Weaver, T. E. Vaughan, R. K. Adair, and R. D. Astumian, *Biophysical journal* **75**, 2251 (1998).
- [133] J. S. Kelso, *Dynamic patterns: The self-organization of brain and behavior*. (MIT press, 1997).
- [134] S. Manicka and M. Levin, *Philos Trans R Soc Lond B Biol Sci* **374**, 20180369 (2019).
- [135] P. McMillen, M. J. Oudin, M. Levin, and S. L. Payne, *Frontiers in Cell and Developmental Biology* **9**, 739024 (2021).
- [136] T. Berleth and T. Sachs, *Current opinion in plant biology* **4**, 57 (2001).
- [137] P. McMillen, M. J. Oudin, M. Levin, and S. L. Payne, *Front Cell Dev Biol* **9**, 739024 (2021).
- [138] S. Caviglia and E. A. Ober, *Current opinion in cell biology* **54**, 106 (2018).
- [139] M. Levin, G. Pezzulo, and J. M. Finkelstein, *Annu Rev Biomed Eng* **19**, 353 (2017).
- [140] E. M. De Robertis, *Mech Dev* **126**, 925 (2009).
- [141] T. Bouwmeester, *International Journal of Developmental Biology* **45**, 251 (2001).
- [142] R. Harland and J. Gerhart, *Annu Rev Cell Dev Biol* **13**, 611 (1997).
- [143] L. Wolpert, *Curr Top Dev Biol* **117**, 597 (2016).
- [144] J. Hans, *Cymatics: A Study of Wave Phenomena and Vibration* (MACROmedia Publishing, 2001).
- [145] Y. Hasegawa, *Nature Communications* **14**, 2828 (2023).
- [146] S.-i. Amari, *Neurocomputing* **5**, 185 (1993).
- [147] K. Asami and A. Irimajiri, *Physics in Medicine & Biology* **45**, 3285 (2000).
- [148] D. Das, F. A. Kamil, K. Biswas, and S. Das, *RSC Advances* **4**, 18178 (2014).
- [149] N. Nasir and M. Al Ahmad, *Journal of Engineering* **2020**, 9475490 (2020).
- [150] T. M. Cover, *Elements of information theory* (John Wiley & Sons, 1999).
- [151] R. G. James, C. J. Ellison, and J. P. Crutchfield, *Journal of Open Source Software* **3**, 738 (2018).
- [152] S. Manicka and M. Levin, *Entropy* **24** (2022).

- [153] M. Riedmiller and H. Braun, in *Proc. of ISCIS VII*, Universitat (Citeseer, 1992).
- [154] D. J. Harraway, *Crystals, Fabrics and Fields- Metaphors of Organicism in Twentieth-century Developmental Biology* (Yale University Press, New Haven and London, 1976).
- [155] M. Levin, *Biological Theory* (2020).
- [156] J. B. Green and J. Sharpe, *Development* **142**, 1203 (2015).
- [157] J. Cooke and E. C. Zeeman, *J. Theor. Biol* **58**, 455 (1976).
- [158] H. Meinhardt, *Rep Prog Phys* **55**, 797 (1992).
- [159] T. Fukumoto, I. P. Kema, and M. Levin, *Curr Biol* **15**, 794 (2005).
- [160] T. Fukumoto, R. Blakely, and M. Levin, *Dev Neurosci* **27**, 349 (2005).
- [161] A. T. Esser, K. C. Smith, J. C. Weaver, and M. Levin, *Dev Dyn* **235**, 2144 (2006).
- [162] C. A. Anastassiou and C. Koch, *Curr Opin Neurobiol* **31**, 95 (2015).
- [163] S. A. Weiss and D. S. Faber, *Front Neural Circuits* **4**, 15 (2010).
- [164] G. Ruffini, R. Salvador, E. Tadayon, R. Sanchez-Todo, A. Pascual-Leone, and E. Santarnecchi, *PLoS computational biology* **16**, e1007923 (2020).
- [165] C. Hesp, *Phys Life Rev* **36**, 40 (2021).
- [166] S. M. Busse, P. T. McMillen, and M. Levin, *Development* **145** (2018).
- [167] T. B. Kornberg and S. Roy, *Trends Cell Biol* **24**, 370 (2014).
- [168] P. Husbands, T. Smith, N. Jakobi, and M. O'Shea, *Connection Science* **10**, 185 (1998).
- [169] A. M. Turing, *Bulletin of mathematical biology* **52**, 153 (1990).
- [170] B. M. Stramer, *Cells & Development* **177**, 203883 (2024).
- [171] H. Pauly and H. Schwan, *Biophysical journal* **6**, 621 (1966).
- [172] K. Asami, Y. Takahashi, and S. Takashima, *Biochimica et Biophysica Acta (BBA)-Molecular Cell Research* **1010**, 49 (1989).
- [173] V. P. Andreev, *PloS one* **8**, e61884 (2013).
- [174] V. P. Pai, G. Zhang, and M. Levin, *Bioelectricity* **6**, 65 (2024).
- [175] V. P. Pai, J. M. Lemire, J. F. Pare, G. Lin, Y. Chen, and M. Levin, *The Journal of Neuroscience* **35**, 4366 (2015).
- [176] V. P. Pai, J. M. Lemire, Y. Chen, G. Lin, and M. Levin, *The International journal of developmental biology* **59**, 327 (2015).
- [177] J. Gunawardena, *BMC Biol* **12** (2014).
- [178] D. Lobo, M. Solano, G. A. Bubenik, and M. Levin, *J R Soc Interface* **11**, 20130918 (2014).
- [179] A. Mordvintsev, C. Olah, and M. Tyka, *Google Research* **2** (2015).
- [180] D. Hechavarria, A. Dewilde, S. Braunhut, M. Levin, and D. L. Kaplan, *Med. Eng. Phys.* **32**, 1065 (2010).
- [181] N. J. Murugan *et al.*, *Sci Adv* **8**, eabj2164 (2022).
- [182] M. R. Ebrahimkhani and M. Levin, *iScience* **24**, 102505 (2021).
- [183] J. J. Velazquez, E. Su, P. Cahan, and M. R. Ebrahimkhani, *Trends Biotechnol* **36**, 415 (2018).
- [184] R. D. Kamm *et al.*, *Apl Bioeng* **2**, 040901 (2018).
- [185] B. P. Teague, P. Guye, and R. Weiss, *Cold Spring Harbor perspectives in biology* **8** (2016).